

Late-Stage Generalization Collapse in Grokking: Detecting anti-grokking with WeightWatcher

Hari K. Prakash¹ Charles H. Martin²

Abstract

Memorization in neural networks lacks a precise operational definition and is often inferred from the grokking regime, where training accuracy saturates while test accuracy remains very low. We identify a previously unreported third phase of grokking in this training regime: *anti-grokking*, a late-stage collapse of generalization.

We revisit two canonical grokking setups: a 3-layer MLP trained on a subset of MNIST and a transformer trained on modular addition, but extended training far beyond standard. In both cases, after models transition from pre-grokking to successful generalization, test accuracy collapses back to chance while training accuracy remains perfect, indicating a distinct post-generalization failure mode.

To diagnose anti-grokking, we use the open-source WeightWatcher tool based on HTSR/SETOL theory. The primary signal is the emergence of *Correlation Traps*: anomalously large eigenvalues beyond the Marchenko–Pastur bulk in the empirical spectral density of shuffled weight matrices, which are predicted to impair generalization. As a secondary signal, anti-grokking corresponds to the average HTSR layer quality metric α deviating from 2.0. Neither metric requires access to the test or training data.

We compare these signals to alternative grokking diagnostic, including ℓ_2 norms, Activation Sparsity, Absolute Weight Entropy, and Local Circuit Complexity. These track pre-grokking and grokking but fail to identify anti-grokking. Finally, we show that Correlation Traps can induce catastrophic forgetting and/or prototype memorization, and observe similar pathologies in large-scale LLMs, like OSS GPT 20/120B.

¹University of California San Diego, Data Science and Engineering
²Calculation Consulting, San Francisco, CA. Correspondence to: Hari K. Prakash <hpaprakash@ucsd.edu>, Charles H. Martin <charles@calculationconsulting.com>.

1. Introduction

Grokking is an intriguing phenomenon where a neural network achieves near-perfect training accuracy quickly, yet the test accuracy lags significantly, often near chance level, before abruptly surging towards high generalization (Power et al., 2022). Figure 1 illustrates this for a depth-3, width-200 ReLU MLP trained on a subset of MNIST.¹

To dissect this phenomenon and uncover deeper dynamics, we use the open-source WeightWatcher tool (WW), which implements layer quality metrics derived from theory (HTSR, SETOL). (Martin & Hinrichs, 2025; Martin & Mahoney, 2021; Martin et al., 2021) The tool examines the empirical spectral density (ESD) of individual layer weight matrices (\mathbf{W}), providing insight into both the correlation structure, which is associated with good generalization, and statistical atypicalities, which hurt the model. Specifically, we monitor 2 WW metrics, the number of *Correlation Traps*, and the heavy-tailed power law (PL) exponent α .

To study grokking, we reproduce two classic experiments (Liu et al., 2022; Nanda et al., 2023): (i) a 3-layer MLP trained on a subset of MNIST (with weight decay, $WD=0$, and without, $WD>0$) and (ii) a small transformer trained to learn modular addition (MA). We run both, however, significantly longer than typically examined. We observe that after each model has transitioned from pre-grokking to grokking (successful generalization), test accuracy collapses back to chance while training accuracy remains perfect. We denote this new phase **anti-grokking**. Superficially, anti-grokking resembles pre-grokking (perfect train / poor test). But they are very different, both from each other and in different models.

Using the WW tool, we can readily identify all three phases of grokking directly from the layer ESDs.

First, the anti-grokking phase is strongly associated with the presence of numerous Correlation Traps in both models, exactly as predicted by theory (Martin & Hinrichs, 2025).

Second, the layer α distinguishes the kind of memorization

¹This paper is a substantially extended version of our earlier ICML workshop paper (Prakash & Martin, 2025).

seen in the pre-grokking phase in each model, tracks the transition into the grokking phase in both, and is correlated with a subsequent decrease in generalization in the anti-grokking phase. In the MLP model, α is a secondary but clear signal; in the MA case, however, because the model overfits the data in all phases, the α signal is distorted and one needs to also inspect the layer ESDs visually.

For comparative context, we also investigate several other methodologies:

1. **Weight Norm Analysis:** Motivated by studies like Liu et al. (Liu et al., 2022), we examine the ℓ_2 norm of the weights. We observe that grokking occurs even without weight decay (leading to an increasing norm), suggesting weight norm alone is not a complete explanation, confirming subsequent findings. (Golechha, 2024)
2. **Grokking Progress Measures:** We utilize metrics proposed by Golechha (Golechha, 2024). Activation Sparsity, Absolute Weight Entropy, and Approximate Local Circuit Complexity, which capture broader structural and functional changes in the network during training.

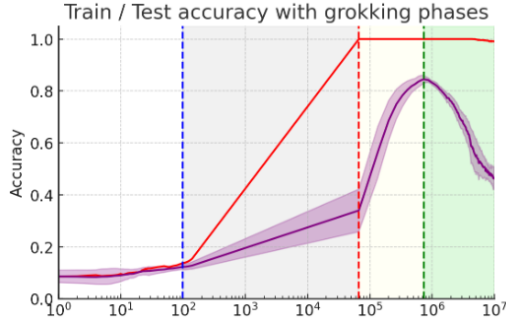


Figure 1. The three phases of grokking. Training curves for a depth-3, width-200 MLP on MNIST. The initial **pre-grokking** phase (grey): training accuracy (red line) surges at 10^2 steps, saturating between $10^4 - 10^5$ steps, while test accuracy (purple line) remains low; the **grokking** phase (yellow): with test accuracy rapidly increasing after $\sim 10^5$ steps, and reaching a maximum at 10^6 steps; and the newly revealed late-stage **anti-grokking** phase (green): test accuracy collapses (to 0.5).

Our Contributions: Our work makes several related contributions that help explain the underlying mechanisms associated with the grokking phenomenon:

1. We identify different types of 'memorization' in the pre-grokking phases. In the MLP case, we find each layer shows a weakly-correlated type of memorization, similar to observations of pretrained models, where $\alpha > 2$. In stark contrast, with MA (modular addition), the very-heavy-tailed (VHT) PL structure

extends beyond the tail to the whole ESD, complicating α fits, and indicating that the training data is very-strongly-memorized.

2. At peak grokking, when test accuracy is maximized, in both models, the *average* $\alpha \approx 2$, as predicted by theory, but with some noise in the estimate.
3. By extending training significantly for both models, we identify and characterize **late-stage generalization collapse**: a substantial drop in test accuracy long after grokking, and the presence of numerous Correlation Traps. We call this **anti-grokking**.
4. In the MLP model, the addition of non-zero weight decay, $WD > 0$, suppresses the onset of Correlation Traps and the extent of the test accuracy drop.
5. In the MLP model, we identify the mechanism of the pre-grokking phase. Only a subset of the model layers are well trained (i.e. $\alpha \leq 4$), whereas at least one layer is underfit (i.e. $\alpha \geq 5$). Moreover, the layers can show great variability between training runs, indicating their instability. Importantly, the layer α 's here are distinct from those in the anti-grokking phases. We call this **weakly-correlated memorization**.
6. Anti-grokking is identified with the average layer α significantly deviating from $\alpha \approx 2$. In the MLP model, anti-grokking is identified with one or more the layer $\alpha < 2$, signifying a new kind of overfitting, and as predicted by theory. In the MA model, however, since all the layers are overfit already, the anti-grokking is associated with an increase in $\alpha > 2$, signifying *catastrophic forgetting*.
7. In the MLP model, we show how specific Correlation Traps correspond to memorizing a specific prototype instance of the training data, leading to the model being 'confused'; we call this **prototype overfitting**.
8. In the MA model, at peak grokking, the ESDs are fully PL across the entire density (indicating strong overfitting) and have just one or a few large eigenvalues, as opposed to a fully formed PL tail. This is unique to the MA model; we call this **rule-based memorization**.

2. Related Work

Grokking (Power et al., 2022) is the surprising delayed emergence of generalization well after training accuracy saturates; there is significant research into its underlying mechanisms. Initial studies often explored grokking in algorithmic tasks, frequently linking the phenomenon to the presence of weight decay (WD) which favors simpler, lower-norm solutions (Liu et al., 2022). Other approaches include mechanistic interpretability (Nanda et al., 2023)

and analyses identifying competing memorization and generalization circuits (Varma et al., 2023; Merrill et al., 2023).

Varma et al. defined ‘ungrokking’ as generalization loss when retraining a grokked network on a *smaller* dataset ($D < D_{crit}$), attributing it to shifting circuit efficiencies under WD. In contrast, we observe **late-stage generalization collapse** (‘anti-grokking’) occurring on the *original* dataset after prolonged training $\sim 10^7$ *without* WD ($WD=0$). This distinct phenomenon is not predicted as it falls outside of the crucial weight decay assumption on which it relies.

Grokking studies now include real-world tasks (Golechha, 2024; Humayun et al., 2024). Golechha introduced progress measures (e.g., Activation Sparsity, Absolute Weight Entropy) and notably observed grokking without WD, resulting in increasing ℓ_2 norms, similar to our setup. We use their metrics for comparison but extend training drastically (up to 10^7 steps), revealing the subsequent ‘anti-grokking’ collapse—a phenomenon not reported in their work (even with $WD=0$).

3. WeightWatcher Layer Quality Metrics

The open-source `WeightWatcher` tool (WW) implements several metrics described by both the early HTSR theory and the more recent SETOL theory. (Martin & Mahoney, 2021; Martin et al., 2021; Martin & Hinrichs, 2025) They are based on examining the individual layer spectral densities using techniques adapted from Random Matrix Theory (RMT), and rigorously established by Statistical Mechanics and extensive experimental observations.

Empirical Spectral Density (ESD) For each layer weight matrix $\mathbf{W} \in \mathbb{R}^{N \times M}$, form the *correlation* matrix

$$\mathbf{X} = \frac{1}{N} \mathbf{W}^\top \mathbf{W} \in \mathbb{R}^{M \times M}. \quad (1)$$

Let $\{\lambda_i\}_{i=1}^M$ be the eigenvalues of \mathbf{X} . The ESD is the discrete measure

$$\rho_{emp}(\lambda) = \frac{1}{M} \sum_{i=1}^M \delta(\lambda - \lambda_i). \quad (2)$$

Random Matrix Theory (RMT) If the entries of \mathbf{W} are i.i.d. (and well behaved), then, in the limit $N \rightarrow \infty, M \rightarrow \infty$ with aspect ratio $Q = N/M \geq 1$ fixed, $\rho_{emp}(\lambda)$ converges to the Marchenko–Pastur (MP) density (Marchenko & Pastur, 1967)

$$\rho_{MP}(\lambda) = \begin{cases} \frac{Q}{2\pi\sigma^2} \frac{\sqrt{(\lambda^+ - \lambda)(\lambda - \lambda^-)}}{\lambda}, & \lambda \in [\lambda^-, \lambda^+], \\ 0, & \text{otherwise,} \end{cases} \quad (3)$$

$$\lambda^\pm = \sigma^2 (1 \pm Q^{-1/2})^2. \quad (4)$$

The MP distribution provides a “null model” against which real, trained weight matrices can be compared.

Generally speaking, the layers in a well-trained NN, and even those in a poorly trained one, rarely follow the MP RMT theory. The WW tool looks at each layer weight matrix and characterizes the deviations from the MP RMT distribution, providing both layer quality metrics and visualizations of the ESDs that can be used to analyze the generalization performance of trained NNs. Here, we examine two layer quality metrics: (i) the HTSR PL exponent α , and (ii) the SETOL Correlation Traps.

3.1. Heavy-Tailed Self-Regularization (HTSR)

Prior work shows that the ESD of real-world DNN layers with learned correlations almost never sits entirely within the MP bulk; instead, the right edge decays into a power law (PL) tail. Formally,

$$\rho_{emp}(\lambda) \sim \lambda^{-\alpha}, \quad \lambda_{\min} < \lambda < \lambda_{\max}, \quad (5)$$

with the exponent α quantifying the strength of the correlations. According to the HTSR framework, different ranges of α corresponds to different phases of training and different levels of convergence for each layer:

- $\alpha \gtrsim 5 - 6$: **Random-like or Bulk-plus-Spikes** the spectrum is close to the MP baseline; little task structure is present.
- $2 \lesssim \alpha \lesssim 5 - 6$: **Weak (WHT) to Moderate Heavy (Fat) Tailed (MHT)** Correlations build up; layers are well-conditioned and typically generalize better.
- $\alpha = 2$ **Ideal value**: Corresponds to fully optimized layers in models. Associated with layers in models that generalize best.
- $\alpha < 2$: **Very-Heavy-Tailed (VHT)** Extremely heavy tails indicate overfitting to the training data and often precede and/or are associated with decreases in the generalization / test accuracy. For $\alpha \ll 2$, the PL fit may extend past the tail to the entire ESD.

The lower bound $\alpha = 2$ on the Fat-Tailed phase is a hard cutoff, whereas the upper bound $\alpha \gtrsim 5 - 6$ is looser because it can depend on the aspect ratio Q . The presence of anomalies (i.e Correlation Traps, etc.), however, can interfere with the PL fits of α .

Theoretical justification of α : This is outlined in a new theory, complementary to HTSR, denoted SETOL: *Semi-Empirical Theory of Learning*.(Martin & Hinrichs, 2025)

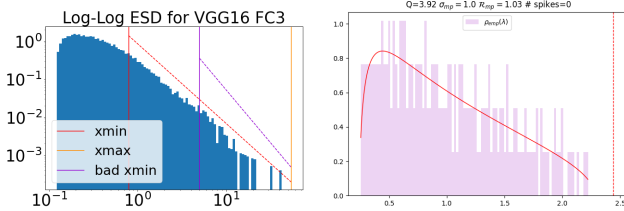


Figure 2. **Left:** Example of the ESD derived from a well-correlated \mathbf{W} (blue) with a power-law tail fit (red), on a **log-log** plot. **Right:** Example of the ESD of \mathbf{W}^{rand} (light purple) with a Marchenko-Pastur (MP) fit (red), shown on a **log-linear** plot.

SETOL posits that the individual layers of a NN will come to thermodynamic equilibrium when the model obtains its optimal generalization accuracy for its training data set. The HTSR PL exponent α then describes the individual contribution a NN layer makes to the total model generalization (called the *Layer Quality*, and where smaller α is better). Importantly, the condition $\alpha = 2$ aligns with an optimal state analogous to a phase boundary between ideal generalization and overfitting (as explained by Wilson’s Exact Renormalization Group). A layer with $\alpha < 2$, and/or one or more Correlation Traps (below), corresponds to states of overfitting, as observed here.

Estimating α . Following (Martin et al., 2021), we fit the tail of ρ_{emp} to a PL 5 through the maximum likelihood estimator (MLE) (Clauset et al., 2009). The start of the PL tail, λ_{\min} , is chosen to minimize the Kolmogorov-Smirnov distance D_{KS} between the empirical and fitted distributions. All calculations are performed with `WeightWatcher` v0.7.5.5 (Martin, 2018-2024), which automates:

- SVD for the singular values σ_i ($\lambda_i = \sigma_i^2$),
- PL fits and D_{KS} tests (including λ_{\min} and λ_{\max}),
- Detecting Correlation Traps.

Figure 2 (Left) shows a PL fit on a log-log scale for a representative layer after training. The plot displays the ESD for a typical NN layer (a histogram or kernel density estimate of $\rho_{\text{emp}}(\lambda)$), the automatically chosen λ_{\min} (xmin, vertical line, red), the λ_{\max} (xmax, vertical line, orange), and the best fit for the PL tail (dashed line, red).

The PL fit is very sensitive to the choice of λ_{\min} , and a poor choice will result in a poorly estimated α . If λ_{\min} is too large (bad xmin, vertical line, purple), then the PL tail is too small and results in a larger α . Selecting λ_{\min} defines the tail alpha (α) and is fully automated using the open-source `WeightWatcher` tool. (Martin, 2018-2024)

Note that in MA model (see Fig. 18), it is very hard to get a reliable PL fit to the tail because the entire ESD is clearly VHT PL, with an effective (full ESD) PL exponent $\alpha \ll 2$.

Significance for Grokking/Anti-Grokking. Across the MLP experiments, the trajectory $\alpha(t)$ proves to be a highly sensitive indicator of the network’s generalization state: large drops toward $\alpha \approx 2$ coincide with the onset of grokking, while a further fall below $\alpha < 2$ foreshadows (and then characterizes) the “anti-grokking” collapse.

3.2. SETOL and Correlation Traps

The SETOL theory predicts that the onset of **Correlation Traps** will induce a phenomenon like anti-grokking (generalization collapse). Such traps are specific atypicalities in the weight matrix elements. What are they and how are they detected using `WeightWatcher`?

If we randomize a layer weight matrix elementwise,

$$\mathbf{W} \rightarrow \mathbf{W}^{\text{rand}}, \quad (6)$$

we then expect the ESD of \mathbf{W}^{rand} to be well-fit by an MP distribution because the elements $W_{i,j}$ should now be uncorrelated and distributed randomly; See Figure 2 (Right). SETOL argues that deviations from this are significant and informative. To identify these deviations, we compare the randomized layer ESDs against the MP distribution at the different stages of training to assess deviations from randomness. We identify these deviations as anomalously large eigenvalues in the underlying \mathbf{W}^{rand} . Such eigenvalues are called Correlation Traps, λ_{trap} , when they extend well beyond the bulk edge λ_{rand}^+ of the best fit MP distribution:

$$\text{Correlation Trap: } \lambda_{\text{trap}} \gg \lambda_{\text{rand}}^+ \quad (7)$$

For more details, see the Appendix E, and the SETOL monograph (Martin & Hinrichs, 2025).

The `WeightWatcher` tool detects Correlation Traps automatically; it randomizes \mathbf{W} elementwise, then performs automated MP fits by estimating the variance σ_{MP}^2 of the underlying randomized matrix \mathbf{W}^{rand} , finding the fit that best describes the bulk of its ESD of \mathbf{W}^{rand} . It then finds all eigenvalues λ_{trap} that are significantly larger (i.e. beyond the Tracy-Widom fluctuations) of the MP bulk edge λ_{rand}^+ of the ESD of \mathbf{W}^{rand} . Figure 3 depicts two layers from the models studied here with Correlation Traps.

For additional statistical validation, here, we also use the Kolmogorov-Smirnov (KS) test to quantify the dissimilarity between the ESD of \mathbf{W}^{rand} and its best MP fit. A large difference, combined with a visual inspection of the ESDs, along with a potentially lower-quality α fit, indicates the presence of one or more Correlation Traps.

3.3. Other Benchmarked Metrics

We benchmarked our MLP findings against the ℓ_2 weight norm and several Grokking progress diagnostics proposed

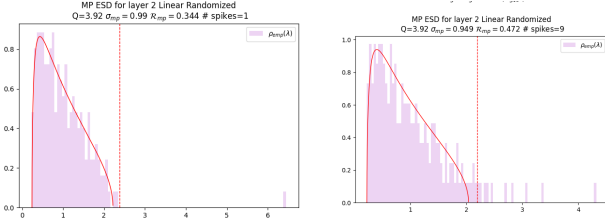


Figure 3. Examples of Correlation Traps. ESDs of \mathbf{W}^{rand} (light purple) of Layer 2 compared to an MP fit (red). Correlation traps λ_{trap} appear as spikes to the right of the MP bulk (log x-axis). **Left: Right Before Collapse** ($\sigma_{mp} \approx 0.9879$; KS $p \approx 4 \times 10^{-13}$). A single dominant trap at $\lambda_{trap} \approx 10^{6.5}$. **Right: Final Generalization Collapse** (KS $p \approx 1.9 \times 10^{-5}$). Multiple traps $\lambda_{trap} \in [10^{2.5}, 10^{6.5}]$.

earlier. In total, we included:

- ℓ_2 Weight Norm ($\|\mathbf{W}\|_2$)
- Activation Sparsity (Λ_{AS})
- Absolute Weight Entropy ($H_{abs}(\mathbf{W})$)
- Approximate Local Circuit Complexity (Λ_{LC})

See Appendix B for further discussion.

4. MLP Experiment: Results and Analysis

Our primary signal for detecting anti-grokking is (SETOL) Correlation Traps, whereas our secondary, weaker signal is the (HTSR) α . We discuss the HTSR α results first, compare these to the other proposed grokking measures, and, finally, discuss the Correlation Traps.

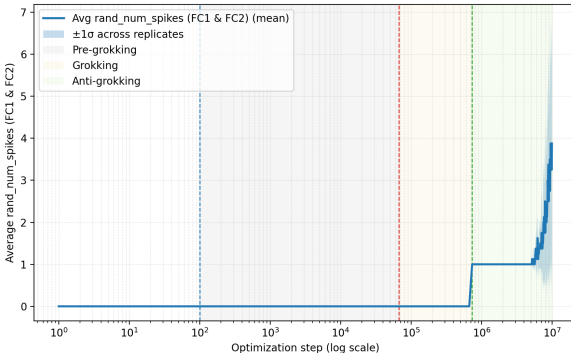


Figure 4. Average Correlation Traps across layers during optimization steps. The increase in the number of traps coincides with the "anti-grokking" performance drop seen in Fig. 1 at 1M steps. This is our primary signal for anti-grokking,

4.1. WeightWatcher Metrics for Tracking Grokking

HTSR layer quality metric α : The HTSR α reveals critical dynamics missed by other measures. Figure 5 shows the evolution of α averaged across layers FC1 and FC2.

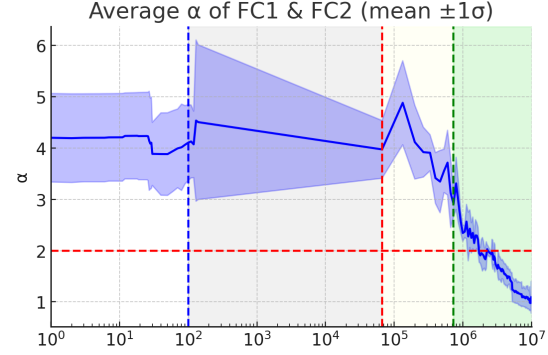


Figure 5. Average α across layers during optimization. Note the drop below the critical threshold $\alpha = 2$, coinciding with the "anti-grokking" performance drop seen in Fig. 1 after $\sim 1M$ steps. This is our secondary signal for anti-grokking. From Figure 11.

Table 1. Layer-wise and average HTSR α exponents. At the right edge of each grokking phase: Pre-grokking $\sim 10^5$ steps, Grokking $\sim 10^6$ steps, and Anti-grokking $\sim 10^7$ steps. For the zero-weight-decay (WD=0) experiment; values are taken from Fig. 5. Various seeds are used and variability in initialization, optimizer trajectory may occur.

Layer	Pre-grokking	Grokking	Anti-grokking
FC1 α	5.0 ± 0.7	3.6 ± 0.5	0.9 ± 0.4
FC2 α	2.9 ± 0.7	2.3 ± 0.2	1.3 ± 0.3
Avg. α	4.0 ± 0.6	2.9 ± 0.2	1.1 ± 0.3

Initially, α is high, reflecting random-like weights. As training progresses and the network begins to fit the training data, α decreases. The sharp drop towards the optimal (fat-tailed) regime ($2 \lesssim \alpha \lesssim 5-6$) coincides with grokking phase (Figure 1, 10^4 - 10^5 steps).

As training continues, however, and into the millions of steps, α consistently dips below 2, entering the VHT regime. This occurs notably in the second fully connected layer (FC2, see Figure 11). This drop of $\alpha < 2$ indicates a sub-optimal layer with overly strong correlations, occurring just after the significant drop in test accuracy, the anti-grokking phase, observed after 10^6 steps in Figure 1.

HTSR theory predicts optimal test performance when all layers reach $\alpha \approx 2$, but only late in training here. We attribute this delay to the small dataset, which requires extended optimization for full layer convergence; however, by the time $\alpha \approx 2$ is reached, Correlation Traps emerge, degrading test performance and inducing anti-grokking.

Together, these observations highlight the unique sensitivity of the HTSR α metric. This metric not only identifies the grokking transition but also provides an early warning for the subsequent instability and the novel anti-grokking phenomenon, highlighting pathological correlation struc-

tures/overfitting forming deep into training.

Here, the HTSR α is a weaker but important secondary signal for anti-grokking; a much stronger, more general signal is the presence of Correlation Traps, as shown in Figure 4. But first, we examine other metrics from the literature.

Other comparative metrics: In contrast, the other comparative metrics capture the initial training and grokking phases but fail to predict the late-stage generalization collapse. Figure 6 displays the Activation Sparsity, Absolute Weight Entropy, and Approximate Local Circuit Complexity (Λ_{LC}). While these metrics show clear trends during the initial learning and grokking phases (e.g., changes in sparsity and complexity), their trajectories become relatively stable or lack distinct features corresponding to the dramatic performance drop seen during "anti-grokking".

For example, Λ_{LC} remains relatively flat in the late-stages up until some noise at the end, offering no warning of the impending collapse. In contrast, the onset of the collapse is immediately detected by the onset of numerous Correlation Traps, and verified (a little later) with average $\alpha < 2$.

Similarly, the Activation Sparsity (Λ_{AS}) shows an inflection around just before peak test accuracy and does detect grokking, it generally continues its upward trend in the late-stage collapse. At peak test accuracy, however, it has a similar value as peak anti-grokking. Moreover, in the control $WD > 0$ case, the Λ_{AS} also shows an inflection point, but there is only very slight anti-grokking, and this just indicates that some unknown transitional change has occurred.

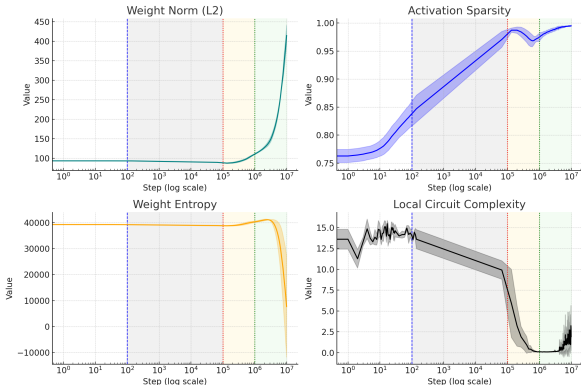


Figure 6. Alternative progress measures (Golechha (Golechha, 2024)) vs. optimization steps. Top: Activation Sparsity. Middle: Absolute Weight Entropy. Bottom: Approximate Local Circuit Complexity. While these metrics show changes during the initial training and grokking phases (Activation Sparsity for example), they do not clearly delineate onset or magnitude of the late-stage "anti-grokking" performance dip observed after 10^6 steps.

In the $WD=0$ case, Λ_{AS} generally increases throughout training (Figure 6), seemingly tracking the pre-grokking and grokking phases, however, it fails the negative control

Table 2. Average # Correlation Traps in FC1/FC2 at the right edge of three phases: Pre-grok ($\sim 10^5$ steps), Grok (10^6), Anti-grok (10^7). Without weight decay ($WD=0$) and with ($WD>0$).

Setting, Layer	Pre-Grokking	Grokking	Anti-Grokking
WD=0, FC1	0 ± 0	0 ± 0	7.5 ± 5.6
WD=0, FC2	0 ± 0	0 ± 0	1 ± 0
WD>0, FC1	0	0	2.0 ± 0.0
WD>0, FC2	0	0	1.0 ± 0.0

in the anti-grokking phase because it continues to increase in the same way as in pre-grokking. Prior studies have linked activation sparsity to generalization (Li et al., 2023; Merrill et al., 2023; Peng et al., 2023) and reported specific dynamics such as plateauing before grokking (Golechha, 2024) or an increase preceding a rise in test loss (Huesmann et al., 2021). Specifically, we observe a subtle inflection or dip in Λ_{AS} coinciding with the point of maximum test accuracy before a slight increase. While this feature appears to mark a shift around peak test accuracy, its specific predictive utility for subsequent generalization dynamics is questionable. In other words, without knowing the proper sparsity cutoff, it is impossible to determine if increasing Λ_{AS} corresponds to pre-grokking or anti-grokking. In contrast, because the HTSR $\alpha = 2$ is a theoretically established universal cutoff, it can distinguish the two phases.

4.2. SETOL Correlation Traps and Anti-Grokking

The strongest signal we have for anti-grokking is the sudden onset of Correlation Traps in both layers, in both the cases with ($WD > 0$) and without $WD=0$ weight decay. As described in Section 3.1, we analyze the eigenvalues $\{\lambda_i\}$ of the randomized weight matrices \mathbf{W}^{rand} derived from each layer's weight matrix \mathbf{W} for layers FC1 and FC2.

First, as clearly shown in Figure 4, for the $WD=0$ case, numerous Correlation Traps suddenly appear right at the onset of the anti-grokking phase. Second, as shown in Table 2, for layers FC1 and FC2, and for both WD settings, neither layer shows evidence of Correlation Traps until the anti-grokking phase. Moreover, there are significantly more traps in the $WD=0$ case, which coincides with the much stronger anti-grokking observed. Finally, further statistical analysis for the FC2 layers is provided in Appendix E. The presence of Correlation Traps, combined with $\alpha < 2$ (later), is a definitive signal indicating the model is deep in the anti-grokking phase. So what are the traps?

Correlation Traps and Prototype Memorization We can identify certain Correlation Traps with the MLP model overfitting to specific prototypes of the training data. As shown in Figure 7, the leading right singular vector $v^{(1)}$ of FC1 evolves from unstructured noise (pre-grokking) to

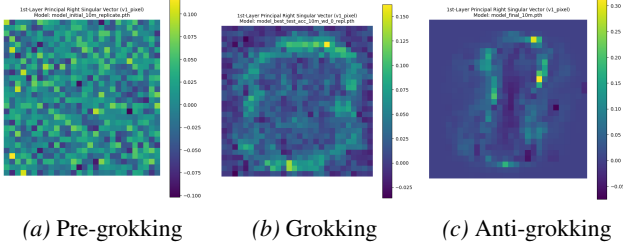


Figure 7. Prototype-Memorization. Largest right singular vector $v^{(1)}$ of W_1 in pixel space. $v^{(1)}$ evolves from (i) unstructured noise in pre-grokking, to (ii) a smooth global ring-like template during grokking, to (iii) localized, digit-shaped templates (resembling an “8”) in anti-grokking.

a smooth, global template at peak generalization, and finally into highly localized, digit-shaped patterns in the anti-grokking phase. These localized structures indicate that the model has begun encoding specific training prototypes at the level of individual layers, rather than learning a generalizable representation. This is described in more detail the Appendix, Section G. Furthermore W_1 rows show clear digit memorization as seen in Figure 15. The trap(s) causes the MLP model to systematically mispredict the test examples, and is fundamentally different from the weakly-correlated overfitting in the pre-grokking phase.

5. MA Experiment: Results and Analysis

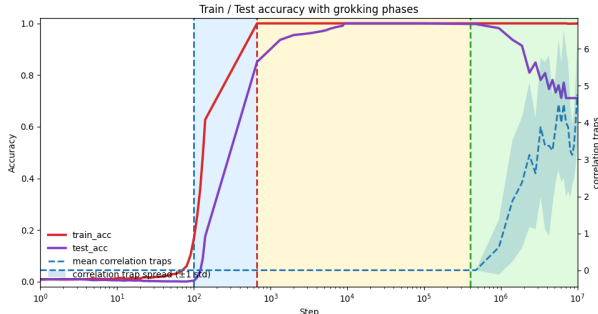


Figure 8. Average Correlation Traps across layers during optimization steps. The increase in the number of traps coincides with the anti-grokking drop in test performance (purple).

We summarize our results on the Modular Addition (MA) experiment below; the Appendix provides more details.

As with the MLP experiment, the MA experiment shows an anti-grokking phase when trained significantly longer than the standard setup. And, as with the MLP case, anti-grokking is readily detected by the onset of numerous Correlation Traps. This is clearly seen in Figure 8, and in Table 7. Moreover, the onset of the grokking phase is also associated with the layer average HTSR PL $\alpha \approx 2$.

The structure of the layer ESDs, however, are significantly different from that expected from the MLP case, and indi-

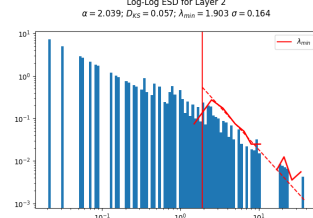


Figure 9. Rule-based Memorization. Grokking embedding layer ESD. Empirical spectral density (ESD) of $\mathbf{W}_{\text{embed}}$ (log-log) with a PL tail fit. During grokking, the tail fit is strongest (low D_{KS}) and α is near the HTSR optimum, $\alpha \approx 2$. From Figure 18d.

cate that in all phases nearly all layers are strongly overfit to the training data. See Figure 9. Specifically, while `WeightWatcher` can fit the tail of the ESDs to a PL, and in the grokking case the PL fit is very good ($\alpha \approx 2$, $D_{\text{KS}} = 0.05$), never-the-less, the ESD in Figures 18 and 18f are clearly VHT PL across the entire spectrum.

Moreover, in the grokking phase, many layers have only 1 or a few very large eigenvalues, as opposed to a well formed PL tail. We call this as **rule-based memorization**.

As shown in Figure 18e, with the Correlation Traps, the PL tail shrinks and the fit reverts back to a larger (not smaller) $\alpha = 3.138$. This is typical here, and because of this, the traps appear to be inducing *catastrophic forgetting*.

6. Conclusion

This study investigated the well-known grokking phenomenon in neural networks (NN) using the open-source `WeightWatcher` tool (Martin, 2018-2024). We study the long-term generalization dynamics of the grokking phenomenon in an MLP model on MNIST, both with weight decay ($\text{WD} > 0$) and without ($\text{WD} = 0$), and in the classic modular addition (MA) experiment using a small transformer.

We compare the application of the tool’s layer quality metrics, the HTSR α metric, and the presence of Correlation Traps from the more recent SETOL theory. We track the number of traps and the layer α across optimization steps, and visually inspect the ESDs as needed.

For both the MLP model (notably in the $\text{WD} = 0$ setting), and for the MA model, we observe a novel **late-stage generalization collapse**, called **anti-grokking**. This collapse is characterized by a significant drop in test accuracy despite sustained perfect training accuracy (and a large ℓ_2 norm) after extensive training (up to 10^7 steps).

Our primary finding is that we can reliably detect this new anti-grokking phases by observing the onset of numerous Correlation Traps in one or more layers. The effect of such traps is predicted by the recently developed SETOL statistical mechanics theory underlying the `WW` tool.

Secondarily, we find that at or near peak grokking, as predicted by theory, the average layer $\alpha \approx 2$ in both models, as predicted, and, moreover, the later anti-grokking phase is seen in the MLP case by 1 or more layers with $\alpha < 2$.

For the MLP models, we compare these metrics to the ℓ_2 norm and several previous proposed grokking progress measures (Liu et al., 2022; Golechha, 2024), and for both settings ($WD=0$, $WD>0$). Previous work has attempted to explain grokking (using the ℓ_2 norm), but only succeeds in the presence of weight decay (WD), and has been unable to explain grokking without weight decay. We examined 3 other grokking progress measures, plus the ℓ_2 norm, including Activation Sparsity Λ_{AS} , Absolute Weight Entropy $H_{abs}(W)$, and Approximate Local Circuit Complexity Λ_{LC} . Although Λ_{AS} and Λ_{LC} captured the first 2 grokking phases, and do change at the anti-grokking transition, they fail to unambiguously predict anti-grokking.

We propose a new explanation of the grokking phenomenon. In the pre-grokking phase, where only training accuracy saturates, only a subset of layers converge ; and not fully. Crucially, layers most relevant for generalization have not yet converged. During the grokking phase, when test accuracy is maximal, important layers converge strongly, with average α eventually approaching the optimal value $\alpha \approx 2.0$, as predicted (Martin & Hinrichs, 2025). In the anti-grokking phase, test accuracy drops because one or more layers exhibit Correlation Traps (and sometimes rank collapse) which hurt generalization.

The MLP and MA models both exhibit this grokking behavior in their layers, but the nature of memorization is very different. In the MLP model, pre-grokking memorization starts as weakly-correlated, and in the anti-grokking phase, Correlation Traps cause overfitting to specific training data prototypes. In the MA model, all of the layers are very-strongly overfit to the training data in all phases, but correlations still concentrate into a fat PL tail at peak grokking. In anti-grokking, numerous Correlation Traps also appear, but here causing catastrophic forgetting.

We consider the implications of observing numerous Correlation Traps in the anti-grokking phase, both in the MLP and MA models. The 'traps' are anomalous rank-one (or greater) perturbations in the weight matrix \mathbf{W} , causing a large mean-shift in the distribution of elements: $\mathbb{E}[W_{ij}] \rightarrow \text{large}$ and distorting the ESDs and interfering with PL tail fits of α . The large shift in $\mathbb{E}[W_{ij}] \rightarrow \text{large}$ indicates that the distribution of weights is *atypical*. That is, different random samples of the weights could have very different means. And as with any statistical estimator, an atypical distribution will not generalize well, irrespective of the particular mechanism of overfitting (or forgetting).

These results underscore the utility of the open-source

WeightWatcher tool for monitoring and understanding long-term generalization stability across different training schemes and models, with a particular strength in identifying overfitting and catastrophic collapse. For example, in Figure 10, it is observed that production quality LLMs, like the OpenAI OSS GPT20B and 120B models show an unusually large number of layers with $\alpha < 2$ (and Correlation Traps, not shown). These results suggest these anomalies may hurt LLM performance in unpredictable ways.

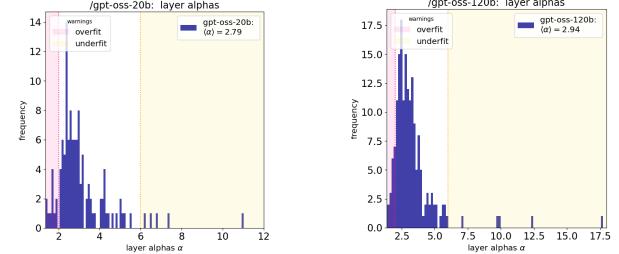


Figure 10. Distribution of WeightWatcher HTSR PL α across layers of gpt-oss-20b and gpt-oss-120b. The dotted vertical lines mark the diagnostic warning thresholds: $\alpha \lesssim 2$ (pink) flags overfitting, while $\alpha \gtrsim 6$ (orange) flags underfitting. Both models exhibit a significant and unusual number of layers with $\alpha < 2$.

7. Limitations

The WeightWatcher HTSR α metric is an empirically-grounded, phenomenological framework, supported rigorously with recently developed SETOL statistical mechanics theory. Still, care must be taken in interpreting the results with α . While well-performing models exhibit α values within the range (e.g., $2 \leq \alpha \leq 6$), and $\alpha \approx 2$ is frequently associated with optimal performance, it is not guaranteed. It is conceivable that models might exhibit α values near or even below 2 (typically indicating over-correlation) yet display suboptimal generalization. As shown here. Other very-well trained models may have layers fairly large $\alpha \gg 2$, as is known. This is not yet fully understood. This highlights that while α provides strong correlational insights into learning phases and stability, the precise mapping of specific α values to absolute performance levels can be context-dependent and is an area for ongoing refinement of the theory. Our work contributes observations within specific phenomena, acknowledging that the broader applicability and predictive nuances when using the WeightWatcher tool and the HTSR and SETOL theories will benefit from continued exploration.

References

Clauset, A., Shalizi, C. R., and Newman, M. E. Power-law distributions in empirical data. *SIAM Review*, 51(4): 661–703, 2009.

Golechha, S. Progress measures for grokking on real-

world tasks, 2024. URL <https://arxiv.org/abs/2405.12755>.

Huesmann, K., Rodriguez, L. G., Linsen, L., and Risse, B. The impact of activation sparsity on overfitting in convolutional neural networks, 2021. URL <https://arxiv.org/abs/2104.06153>.

Humayun, A. I., Balestrieri, R., and Baraniuk, R. Deep networks always grok and here is why, 2024. URL <https://arxiv.org/abs/2402.15555>.

Li, Z., You, C., Bhojanapalli, S., Li, D., Rawat, A. S., Reddi, S. J., Ye, K., Chern, F., Yu, F., Guo, R., and Kumar, S. The lazy neuron phenomenon: On emergence of activation sparsity in transformers. In *The Eleventh International Conference on Learning Representations (ICLR)*, 2023. URL <https://openreview.net/forum?id=TJ2nxciYCk->. arXiv:2210.06313.

Liu, Z., Kitouni, O., Nolte, N. S., Michaud, E. J., Tegmark, M., and Williams, M. Towards understanding grokking: An effective theory of representation learning. In Koyejo, S., (formerly Mohamed), S. K., Agarwal, A., Belgrave, D., Cho, K., and Oh, A. (eds.), *Advances in Neural Information Processing Systems*, volume 35, pp. 34651–34663. Curran Associates, Inc., 2022.

Marchenko, V. A. and Pastur, L. A. Distribution of eigenvalues for some sets of random matrices. *Matematicheskii Sbornik*, 72(114)(4):507–536, 1967.

Martin, C. H. WeightWatcher: Analyze Deep Learning Models without Training or Data. <https://github.com/CalculatedContent/WeightWatcher>, 2018-2024. Version 0.7.5.5 used in this study. Accessed May 12, 2025.

Martin, C. H. and Hinrichs, C. SETOL: A semi-empirical theory of (deep) learning. *arXiv preprint arXiv:2507.17912*, 2025. URL <https://arxiv.org/abs/2507.17912>.

Martin, C. H. and Mahoney, M. W. Implicit self-regularization in deep neural networks: Evidence from random matrix theory and implications for learning. *Journal of Machine Learning Research*, 22(1):165, January 2021. URL <http://jmlr.org/papers/v22/20-410.html>.

Martin, C. H., Peng, T., and Mahoney, M. W. Predicting trends in the quality of state-of-the-art neural networks without access to training or testing data. *Nature Communications*, 12:4122, jul 2021. doi: 10.1038/s41467-021-24025-8. URL <https://doi.org/10.1038/s41467-021-24025-8>.

Merrill, W., Tsilivis, N., and Shukla, A. A tale of two circuits: grokking as competition of sparse and dense subnetworks, 2023. URL <https://arxiv.org/abs/2303.11873>.

Nanda, N., Chan, L., Lieberum, T., Smith, J., and Steinhardt, J. Progress measures for grokking via mechanistic interpretability, 2023. URL <https://arxiv.org/abs/2301.05217>.

Peng, Z., Qi, L., Shi, Y., and Gao, Y. Theoretical explanation of activation sparsity through flat minima and adversarial robustness, 2023. URL <https://arxiv.org/abs/2309.03004>.

Power, A., Burda, Y., Edwards, H., Babuschkin, I., and Misra, V. Grokking: Generalization beyond overfitting on small algorithmic datasets, 2022. URL <https://arxiv.org/abs/2201.02177>.

Prakash, H. K. and Martin, C. H. Grokking and generalization collapse: Insights from htsr theory. *arXiv preprint*, arXiv:2506.04434, 2025. URL <https://arxiv.org/abs/2506.04434>.

Varma, V., Shah, R., Kenton, Z., Kramár, J., and Kumar, R. Explaining grokking through circuit efficiency, 2023. URL <https://arxiv.org/abs/2309.02390>.

Appendices

A. MLP Experimental Setup

We train a Multi-Layer Perceptron (MLP) on a subset of the MNIST dataset using the hyperparameters detailed in Table 3. The training subset is constructed by randomly selecting 100 samples from each of the 10 MNIST classes, ensuring a balanced dataset of 1,000 unique training points. This was run on an Nvidia Quadro P2000 and took approximately 11 hours. A considerable part of the time is due to the speed of saving the measures.

Table 3. MLP Experimental hyperparameters used in the study (details in Appendix A).

Parameter	Value
Network Architecture	Fully Connected MLP
Depth	3 Linear layers (Input → Hidden1 → Hidden2 → Output)
Width	200 hidden units per hidden layer
Activation Function	ReLU (Rectified Linear Unit)
Input Layer Size	784 (Flattened MNIST image 28×28)
Output Layer Size	10 (MNIST digits 0-9)
Weight Initialization	Default PyTorch (Kaiming Uniform for weights), parameters scaled by 8.0
Bias Initialization	Default PyTorch (Uniform), then scaled by 8.0
Dataset	MNIST
Training Points	1,000 (100 per class, stratified random sampling)
Test Points	Standard MNIST test set (10,000 samples)
Batch Size	200
Loss Function	Mean Squared Error (MSE) with one-hot encoded targets
Optimizer	AdamW
Learning Rate (LR)	5×10^{-4}
Weight Decay (WD)	0.0 (for main results), 0.01 (for Appendix D comparison)
AdamW β_1	0.9 (PyTorch default)
AdamW β_2	0.999 (PyTorch default)
AdamW ϵ	10^{-8} (PyTorch default)
Optimization Steps	10^7
Data Type (PyTorch)	‘torch.float64’
Random Seed	0 (for all libraries)
Software Framework	PyTorch
HTSR Tool	WeightWatcher v0.7.5.5 (Martin, 2018-2024)

Note on Weight Decay: The primary results presented in this paper, particularly those demonstrating grokking followed by late-stage generalization collapse (Figure 1), were obtained with weight decay explicitly set to 0. This allows observation of the learning dynamics driven purely by the optimizer and the loss landscape while exhibiting both phenomena, whereas the other proposed measures fail to detect the grokking transition of increasing test accuracy. Runs with non-zero weight decay (e.g., $WD=0.01$, see Appendix D) were also performed for comparison, showing different dynamics but confirming the general utility of HTSR.

B. Comparative Grokking Progress Metrics and Measures

Weight Norm Analysis Following observations that weight decay can influence grokking (Liu et al., 2022), we monitor the ℓ_2 norm of the network’s weights,

$$\|\mathbf{W}\|_2 = \sqrt{\sum_l \|\mathbf{W}_l\|_F^2}, \quad (8)$$

throughout training. We specifically run experiments with weight decay disabled ($WD=0$) to isolate the effect of the optimization dynamics on the norm itself.

Activation Sparsity. For a given layer with activations $b_{i,j}$ (representing the activation of neuron j for input example i), the activation sparsity Λ_{AS} is defined as:

$$A_s = \frac{1}{T} \sum_{i=1}^T \frac{1}{n} \sum_{j=1}^n \mathbf{1}(b_{i,j} < \tau), \quad (9)$$

where T is the number of training examples, n is the number of neurons in the layer, τ is a chosen threshold, and $\mathbf{1}(\cdot)$ is the indicator function. This metric measures neuron inactivity. Prior studies have linked activation sparsity to generalization (Li et al., 2023; Merrill et al., 2023; Peng et al., 2023) and reported specific dynamics such as plateauing before grokking (Golechha, 2024) or an increase preceding a rise in test loss (Huesmann et al., 2021).

Absolute Weight Entropy. For a weight matrix $W \in \mathbb{R}^{m \times n}$, the absolute weight entropy $H_{abs}(W)$ is given by:

$$H_{abs}(W) = - \sum_{i=1}^m \sum_{j=1}^n |w_{i,j}| \log |w_{i,j}|. \quad (10)$$

This entropy quantifies the spread of absolute weight magnitudes. Golechha (Golechha, 2024) suggested its sharp decrease signals generalization.

Approximate Local Circuit Complexity. Let $L^{(W)}(x)$ denote the output logits for input x using weights W , and let $L^{(W')}(x)$ denote the logits when 10% of the weights are set to zero (forming W'). The approximate local circuit complexity, denoted Λ_{LC} , is the summed KL divergence:

$$\Lambda_{LC} = \sum_{k=1}^{N_{data}} \sum_{j \in \mathcal{C}} \Pr(j|L^{(W)}(x_k)) \log \frac{\Pr(j|L^{(W)}(x_k))}{\Pr(j|L^{(W')}(x_k))}. \quad (11)$$

Here, N_{data} is the number of training examples x_k , \mathcal{C} is the set of classes, and $\Pr(j|L(x))$ is the probability of class j derived from the logits $L(x)$ (e.g., via softmax). This measure captures output sensitivity to minor weight perturbations. Lower Λ_{LC} has been linked to stable, generalizable representations (Golechha, 2024).

C. MLP Experiment without Weight Decay

Figure 11 provides the full HTSR layer α for the $WD=0$ experiment, for each layer, plotted for all three phases.

D. MLP Experiment with Weight Decay

To further understand the influence of weight decay on the observed generalization dynamics and the behavior of our tracked metrics, we conducted an experiment identical to our main study ($WD=0$) but with a small amount of weight decay ($WD=0.01$) applied. The training curves and metric evolutions for this $WD=0.01$ experiment are presented in Figures 12, and 13.

A key characteristic of training with weight decay is the tendency for the ℓ_2 norm of the weights to decrease over time, or stabilize at a lower value, which is observed in this experiment (Figure 13). This contrasts with the continuously increasing ℓ_2 weight norm seen in our primary $WD=0$ experiments.

In this $WD=0.01$ regime, the network still achieves a high level of test accuracy. Notably, after the initial grokking phase, the test accuracy slightly decreases and then enters a prolonged plateau, maintaining near peak performance for a significant number of optimization steps (Figure 12). Correspondingly, the average heavy-tail exponent, α , also exhibits the decrease and a distinct plateau around the critical value of $\alpha \approx 2$ during this period (Figure 12, top left panel).

The other progress measures considered—Activation Sparsity and Approximate Local Circuit Complexity—also tend to plateau or stabilize during this phase of peak test performance in the $WD=0.01$ setting (Figure 13). This contrasts with

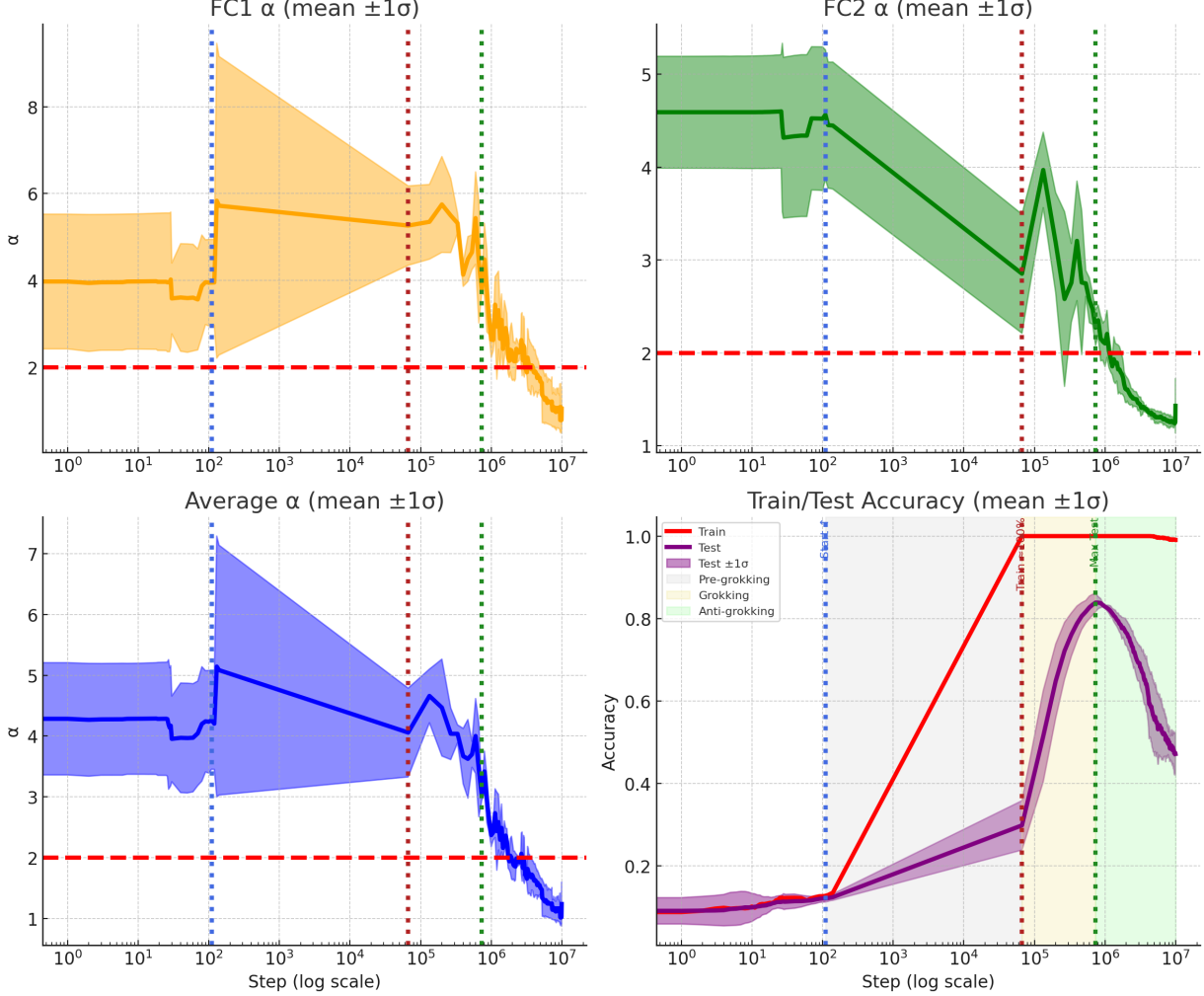
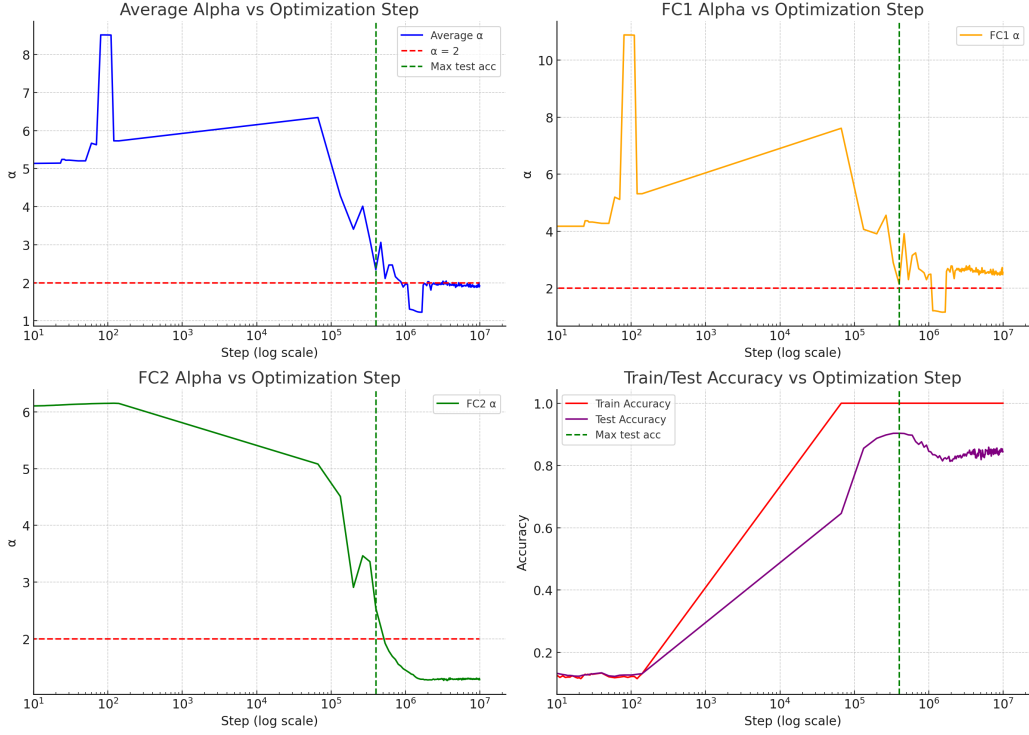
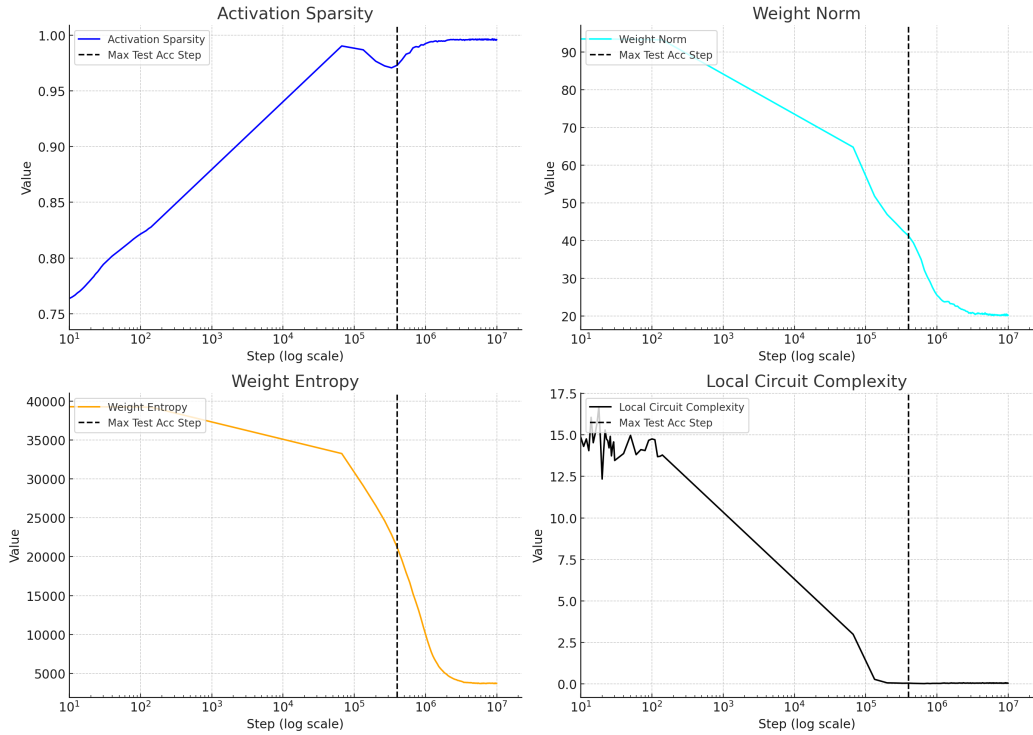


Figure 11. Layer-wise α dynamics and accuracy across training (replicate run). **Top left:** Mean α ($\pm 1\sigma$) for the first fully connected layer (FC1). **Top right:** Mean α ($\pm 1\sigma$) for the second fully connected layer (FC2). **Bottom left:** Mean α averaged across layers. **Bottom right:** Train and test accuracy (mean $\pm 1\sigma$). Vertical dashed lines indicate the transitions between pre-grokking (blue), grokking (red), and anti-grokking (green) phases. The dashed horizontal line at $\alpha = 2$ marks the HTSR/SETOL critical value. During grokking, layer-wise α approaches the optimal regime $\alpha \approx 2$, coinciding with peak test accuracy. In the anti-grokking phase, α drops below 2 in one or more layers, coinciding with generalization collapse.

the $WD=0$ scenario where, despite eventual grokking, the system does not find such a stable long-term plateau and instead proceeds towards a late-stage generalization collapse. The observation that α (and other metrics) plateau in conjunction with peak, stable test accuracy under traditional weight decay settings aligns with some existing understanding of well-regularized training.

While HTSR and the α exponent provide valuable insights in both regimes, its unique capability to signal impending collapse in the absence of weight decay underscores its importance for understanding layer dynamics under various scenarios.


 Figure 12. HTSR α exponent evolution for the MLP trained with WD=0.01.

 Figure 13. Progress measures (Activation Sparsity, Weight Entropy, Circuit Complexity) and ℓ_2 Weight Norm for the MLP trained with WD=0.01.

E. Statistical Analysis and Validation of Correlation Traps

Here, to further validate the presence of Correlation Traps for the zero weight decay $WD=0$ experiment, we report the results of statistical tests designed to determine if the randomized ESD of the \mathbf{W}^{rand} fits an MP distribution or not. Briefly we fit the ESD to a MP distribution and report the fitted variance σ_{mp} , the Kolmogorov-Smirnov (KS) statistic of the fit, and the p-value for the MP fit as the null model. We also report the number of Correlation Traps, as determined using the open-source `WeightWatcher` tool (Martin, 2018-2024). Results for layer FC1 are presented in Table 4. Results for FC2 are similar (not shown). Additional details are provided in the supplementary material.

Table 4. Statistical validation of Correlation Traps. Selected results for layer FC1 at different training stages for zero weight decay ($WD=0$) experiment. MP Variance (σ_{MP}) Kolmogorov-Smirnov (KS) test statistic, p-value for MP fit, and number of detected Correlation Traps. Pre-grokking $\sim 10^5$ steps, Grokking 10^6 steps, and Anti-grokking 10^7 steps,

Model State	MP variance (σ_{mp})	KS Statistic	p-value	# Traps
Pre-Grokking	≈ 1.002	0.0120	≈ 1.0	0
Grokking (Max Test Accuracy)	≈ 0.999	0.0212	≈ 1.0	0
Anti-Grokking (Collapse)	≈ 0.949	0.3044	1.877×10^{-5}	9

Initial Layer State (Pre-Grokking $WD=0$): Immediately after initialization, the network weights are expected to be largely random, and their ESD should conform well to the MP distribution. Figure 2 (Right) shows an MP fit to an ESD from a representative layer \mathbf{W}^{rand} of the newly initialized model. A KS test comparing this empirical ESD to the fitted MP distribution (using $\sigma_{mp} \approx 1.0024$ as estimated by `WeightWatcher`) yielded a KS statistic of 0.0120 and a p-value ≈ 1.0 . This high p-value indicates this ESD is statistically consistent with the MP distribution, as expected.

Best Layer State (Grokking phase $WD=0$): As the network learns and reaches its maximum test accuracy, significant structure develops in the elements of the weight matrices $W_{i,j}$. This can be seen by randomizing the layer weight matrix elementwise, $\mathbf{W} \rightarrow \mathbf{W}^{rand}$, and plotting ESD, and looking for deviations from the theoretical MP distribution. The ESD now typically exhibits a pronounced heavy tail, with eigenvalues extending beyond the bulk region that might be approximated by an MP fit. For our model at peak test accuracy, the KS test against a fitted MP model ($\sigma_{mp} \approx 0.999$) resulted in a KS statistic of 0.0212 and a p-value ≈ 1 . Again, we cannot reject the MP null model.

Final Layer State (Anti-Grokking phase $WD=0$): In the late-stage of training, as the model undergoes generalization collapse and enters an over-correlated state (characterized by $\alpha < 2$), the ESD of \mathbf{W}^{rand} structure continues to reflect a non-random configuration. The KS test for the final model against an MP fit (with an estimated $\sigma_{mp} \approx 2$) yielded a KS statistic of 0.3044 and a p-value of 1.877×10^{-5} Figure 3 (Right). This result, when interpreted jointly with the evidence of the large outliers, further confirms that the network's structure remains significantly different from a random matrix baseline, consistent with the highly correlated or near rank-collapsed state indicated by our HTSR analysis.

These quantitative comparisons demonstrate a transition from an initially random-like state (consistent with MPD) to progressively more structured, non-random states as learning occurs and eventually leads to over-correlation. The inability of the MP distribution to describe these learned features, especially the heavy tails, necessitates the use of tools like the HTSR theory, the PL exponent α , and the open-source `WeightWatcher` tool, to properly characterize these complex correlation structures and their relationship to generalization performance.

F. Conditions for Outliers after Entry-wise Shuffling of a Weight Matrix

Neural-network layer setting. Consider a fully connected layer with weight matrix $W \in \mathbb{R}^{M \times N}$ mapping an N -dimensional input to an M -dimensional output, and aspect ratio

$$\gamma := \frac{M}{N} \in (0, \infty).$$

Notation. For any matrix W set

$$X(W) := \frac{1}{N} W^\top W, \quad \lambda_{\max}(W) := \lambda_{\max}(X(W)).$$

Fix a variance proxy $\sigma^2 > 0$ and define the Marchenko–Pastur (MP) edges

$$\lambda_- := \sigma^2(1 - \sqrt{\gamma})^2, \quad \lambda_+ := \sigma^2(1 + \sqrt{\gamma})^2.$$

Limit convention. As is standard for MP limits, let $N \rightarrow \infty$ with $M/N \rightarrow \gamma$; every limit below is taken along this sequence.

Norm conventions. For $x \in \mathbb{R}^N$, $\|x\|_2$ is the Euclidean norm; for $A \in \mathbb{R}^{M \times N}$, $\|A\|$ is the spectral norm; and for symmetric S , $\lambda_{\max}(S)$ is its top eigenvalue.

Marchenko–Pastur reminder. The MP $_{\sigma^2, \gamma}$ density is

$$\rho_{\text{MP}}(\lambda) = \frac{\sqrt{(\lambda_+ - \lambda)(\lambda - \lambda_-)}}{2\pi \sigma^2 \gamma \lambda} \mathbf{1}_{[\lambda_-, \lambda_+] }(\lambda).$$

Element-wise shuffling (scrambling). Let $\pi : \{1, \dots, M\} \times \{1, \dots, N\} \rightarrow \{1, \dots, M\} \times \{1, \dots, N\}$ be any permutation. The scrambled matrix is

$$W_{\text{rand}} := (W_{ij})_{\pi(i,j)}.$$

Define $A_N := X(W_{\text{rand}}^{(N)})$, so that

$$\lambda_{\max}(A_N) = \lambda_{\max}(X(W_{\text{rand}}^{(N)})).$$

Definition 1 (typical vs. atypical). A sequence $\{W^{(N)}\}$ is *typical* if $\lambda_{\max}(A_N) \rightarrow \lambda_+$, and *atypical* if

$$\liminf_{N \rightarrow \infty} [\lambda_{\max}(A_N) - \lambda_+] > 0.$$

Theorem 1 (single-entry sufficient condition). Assume $M/N \rightarrow \gamma \in (0, \infty)$ and for some index pair (p_N, q_N) ,

$$\frac{|W_{p_N q_N}^{(N)}|}{\sqrt{N}} \xrightarrow[N \rightarrow \infty]{} \theta, \quad \theta > \sigma(1 + \sqrt{\gamma}).$$

Then there exists N_0 such that for all $N \geq N_0$, $\lambda_{\max}(A_N) > \lambda_+$, so the layer is *atypical*.

Proof. Let $a_N := \max_{i,j} |W_{ij}|$. Permuting entries does not change a_N . Choose a column in W_{rand} that contains an entry of magnitude a_N . Denote by $e_{c_N} \in \mathbb{R}^N$ the corresponding standard basis vector (with a 1 in position c_N and zeros elsewhere). Since $\|e_{c_N}\|_2 = 1$, the Rayleigh quotient yields

$$e_{c_N}^\top A_N e_{c_N} = \frac{1}{N} \|W_{\text{rand}} e_{c_N}\|_2^2 = \frac{1}{N} \sum_{i=1}^M |(W_{\text{rand}})_{ic_N}|^2 \geq \frac{a_N^2}{N}.$$

By the Courant–Fischer principle, for any symmetric matrix S ,

$$\lambda_{\max}(S) = \max_{\|x\|_2=1} x^\top S x,$$

hence $\lambda_{\max}(A_N) \geq a_N^2/N$. By the hypothesis,

$$a_N \geq |W_{p_N q_N}^{(N)}| = (\theta + o(1))\sqrt{N},$$

so that $a_N^2/N \rightarrow \theta^2$. Because $\theta > \sigma(1 + \sqrt{\gamma})$, we have

$$\theta^2 > \sigma^2(1 + \sqrt{\gamma})^2 = \lambda_+.$$

Consequently, there exists N_0 such that for all $N \geq N_0$,

$$\lambda_{\max}(A_N) \geq \frac{a_N^2}{N} > \lambda_+.$$

Therefore the layer under this condition is *atypical*.

Connection with the BBP transition. In the classic spiked-covariance model $W = Z + \theta uv^\top$ (rank-one signal plus i.i.d. noise), an eigenvalue separates from the Marchenko–Pastur bulk precisely when

$$\theta^2 = \sigma^2(1 + \sqrt{\gamma})^2.$$

The condition above places the scrambled matrix in the super-critical regime

$$\theta^2 > \sigma^2(1 + \sqrt{\gamma})^2,$$

so an outlier survives even after correlations are destroyed.

Discussion and intuition. Modern empirical work suggests that *stochastic gradient descent* (SGD) can drive a handful of coordinates of a weight matrix toward abnormally large magnitudes, producing *elementwise* heavy-tailed weight distributions[2]. Here, these heavy-tailed elements $W_{i,j}$ appear as rank-one perturbations, or *spikes*, that distort the spectrum of the layer’s Gram matrix; eigenvalues above the MP bulk appear precisely when the test accuracy drops catastrophically.

Entry-wise shuffling deliberately *destroys all remaining correlations* in the weight matrix while preserving the multiset of magnitudes. If a large eigenvalue survives the shuffle, there must be a *pure-magnitude* signal, rendering the layer atypical.

Theorem 1 and BBP shows that the presence of even one entry growing such that

$$\theta^2 > \sigma^2(1 + \sqrt{\gamma})^2,$$

suffices to guarantee such a surviving outlier, confirming the empirical link between unusually large coordinates and atypical spectra.

This is also highlighted in Reference [3], see Section 5.3 (Bulk + Spikes).

References.

1. Jinho Baik, Gérard Ben Arous, and Sandrine Péché. *Phase transition of the largest eigenvalue for nonnull complex sample covariance matrices*. The Annals of Probability, Ann. Probab. 33(5), 1643–1697 (September 2005).
2. M. Gurbuzbalaban, U. Simsekli, and L. Zhu. *The heavy-tail phenomenon in SGD*. In *International Conference on Machine Learning* (ICML), pp. 3964–3975. PMLR, 2021.
3. Charles H. Martin and Michael W. Mahoney. *Implicit self-regularization in deep neural networks: Evidence from random matrix theory and implications for learning*. Journal of Machine Learning Research, 22(165):1–73, 2021.
4. Charles H. Martin and Christopher Hinrichs. *SETOL: A Semi-Empirical Theory of (Deep) Learning*. arXiv preprint arXiv:2507.17912, 2025.

G. Largest Tail Eigenvectors and Correlation Traps

We now analyze the *largest eigenvalues/eigenvectors* of layer Gram matrices and relate them to the *Correlation Traps* detected in the anti-grokking phase. Throughout, for a weight matrix $W \in \mathbb{R}^{M \times N}$ we write

$$X(W) := \frac{1}{N} W^\top W, \quad \lambda_{\max}(W) := \lambda_{\max}(X(W)),$$

and recall the Marchenko–Pastur (MP) upper edge $\lambda_+ = \sigma^2(1 + \sqrt{\gamma})^2$ with $\gamma = M/N$.

We call any eigenpair (λ, v) of $X(W)$ as defined by the start of the power law as a *tail eigenpair*, and when $\lambda > \lambda_+$ for the *scrambled* matrix W_{rand} (entry-wise permutation of W ; see App. F) we call (λ, v) a *trap eigenpair*. These survive after all inter-entry correlations have been destroyed by shuffling.

What could cause traps? App. F proves a simple sufficient condition: if even a single entry satisfies $|W_{p_N q_N}|/\sqrt{N} \rightarrow \theta$ with $\theta > \sigma(1 + \sqrt{\gamma})$, then for all large N , $\lambda_{\max}(X(W_{\text{rand}})) > \lambda_+$. Thus one cause can be *rank-one perturbations in the weight matrix* that create an MP-outlying eigenvalue that *survives* shuffling, i.e., a trap. This is the BBP super-critical regime and constitutes a purely *magnitude-driven* explanation for atypical spectra, independent of correlations.

Empirical evidence for the Structural outlier. Weight-value histograms across checkpoints (initial → best-test → anti-grok) exhibit these structural outliers. For a 3-layer MLP trained on MNIST:

- **First layer** ($W_1 \in \mathbb{R}^{200 \times 784}$). Anti-grokking shows extreme coordinates (e.g., ≈ -14.78 and $\approx +5.67$), well outside the best-test and pre-grok ranges; the bulk remains near zero but with markedly heavier tails.
- **Second layer** ($W_2 \in \mathbb{R}^{200 \times 200}$). Anti-grokking again introduces large coordinates (e.g., ≈ -4.68 , $\approx +1.11$) absent at pre-grok and subdued at best-test(grok).
- **Third layer** ($W_3 \in \mathbb{R}^{10 \times 200}$). We observe outliers such as ≈ -1.61 and $\approx +2.56$ in anti-grokking.

These large coordinates coincide with pronounced increases of the `WeightWatcher` trap statistic in the anti-grokking phase (cf. the trap table in Sec. H, where mean traps rise from ≈ 0 in pre-/grokking to $\approx 4.13 \pm 1.13$ in anti-grokking). Together with the sufficient condition in App. F, these observations support the following chain:

$$\text{Rank-1 perturbations} \implies \text{MP-outlying eigenvalues} \implies \text{trap eigenpairs after shuffling}.$$

From eigenvalues to vectors: what the largest tail vectors look like. Write the thin SVD $W = U\Sigma V^\top$, so the eigenpairs of $X(W)$ are $(\sigma_k^2/N, v_k)$ with v_k the k -th column of V . Hence the *tail vector* v_1 associated with $\lambda_{\max}(W) = \sigma_1^2/N$ lies in the *input space* of W . This makes tail vectors directly interpretable:

- **Layer W_1 .** $X(W_1) = (1/N)W_1^\top W_1$ acts on pixels. The top right singular vector $v^{(1)} \in \mathbb{R}^{784}$ is a pixel-space pattern. Empirically, $v^{(1)}$ evolves from (i) unstructured noise at pre-grokking, to (ii) a smooth, global ring-like template at best-test (grokking), to (iii) *digit-shaped* templates (looks like an 8) in anti-grokking phase. The last stage indicates a strong localized structure consistent with *memorization*.
- **Layer W_2 .** $X(W_2)$ acts on the *output of layer 1*. Its top right singular vector $v^{(2)} \in \mathbb{R}^{200}$ identifies the layer-1 neurons most involved in the dominant correlated mode. Back-projecting $v^{(2)}$ through W_1 to pixel space, $v_{\text{pix}}^{(2)} := v^{(2)\top} W_1 \in \mathbb{R}^{784}$, produces images that, in anti-grokking, again exhibit crisp digit strokes. The largest coefficients of $v^{(2)}$ pick out specific rows of W_1 , and the corresponding receptive fields (rows of W_1 reshaped to 28×28) show clear digit templates in anti-grokking, whereas they are noise-like at pre-grok and remain largely uninterpretable at best-test.
- **Layer W_3 .** $X(W_3)$ acts on the *output of layer 2*. Its top right singular vector $v^{(3)} \in \mathbb{R}^{200}$ highlights the most excited layer-2 units. Back-projecting successively through W_2 and W_1 ,

$$v_{\text{pix}}^{(3)} := v^{(3)\top} W_2 W_1 \in \mathbb{R}^{784},$$

yields pixel-space patterns that sharpen into digit shapes in anti-grokking.

Mechanistic interpretation. In anti-grokking, you get non-random structural outliers; the ESD develops *tail* spikes (large eigenvalues past this edge), and the associated eigenvectors localize onto coordinates resembling a sample or prototype being memorized from the train set. Entry-wise shuffling preserves the large rank-1 perturbations and thus the outlying eigenvalues, converting these localized modes into *trap* modes. The empirical “rows-of- W_1 ” panels show this directly: noise-like at pre-grokking phase, still diffuse at best-test, but in anti-grokking the top rows look like *clear digit templates*, evidencing **digit memorization**.

Practical procedure (used for the figures). For each checkpoint:

1. Compute the SVD of each linear layer: $W_\ell = U_\ell \Sigma_\ell V_\ell^\top$. The *tail vector* for layer ℓ is $v^{(\ell)} := V_\ell[:, 1]$.
2. For W_1 visualize $v^{(1)}$ in pixel space (reshape to 28×28).
3. For W_2 back-project $v^{(2)}$ to pixel space via $v_{\text{pix}}^{(2)} = v^{(2)\top} W_1$ and display the top- k contributing rows of W_1 chosen by the largest coordinates of $v^{(2)}$.
4. For W_3 back-project $v^{(3)}$ through W_2 and W_1 to obtain $v_{\text{pix}}^{(3)}$, and again inspect the top contributors.
5. In parallel, compute $\lambda_{\max}(X(W_\ell))$ and $\lambda_{\max}(X(W_{\ell, \text{rand}}))$ and compare to λ_+ to flag *trap* eigenpairs; relate these to the `WeightWatcher` trap counts and to the HTSR α estimates.

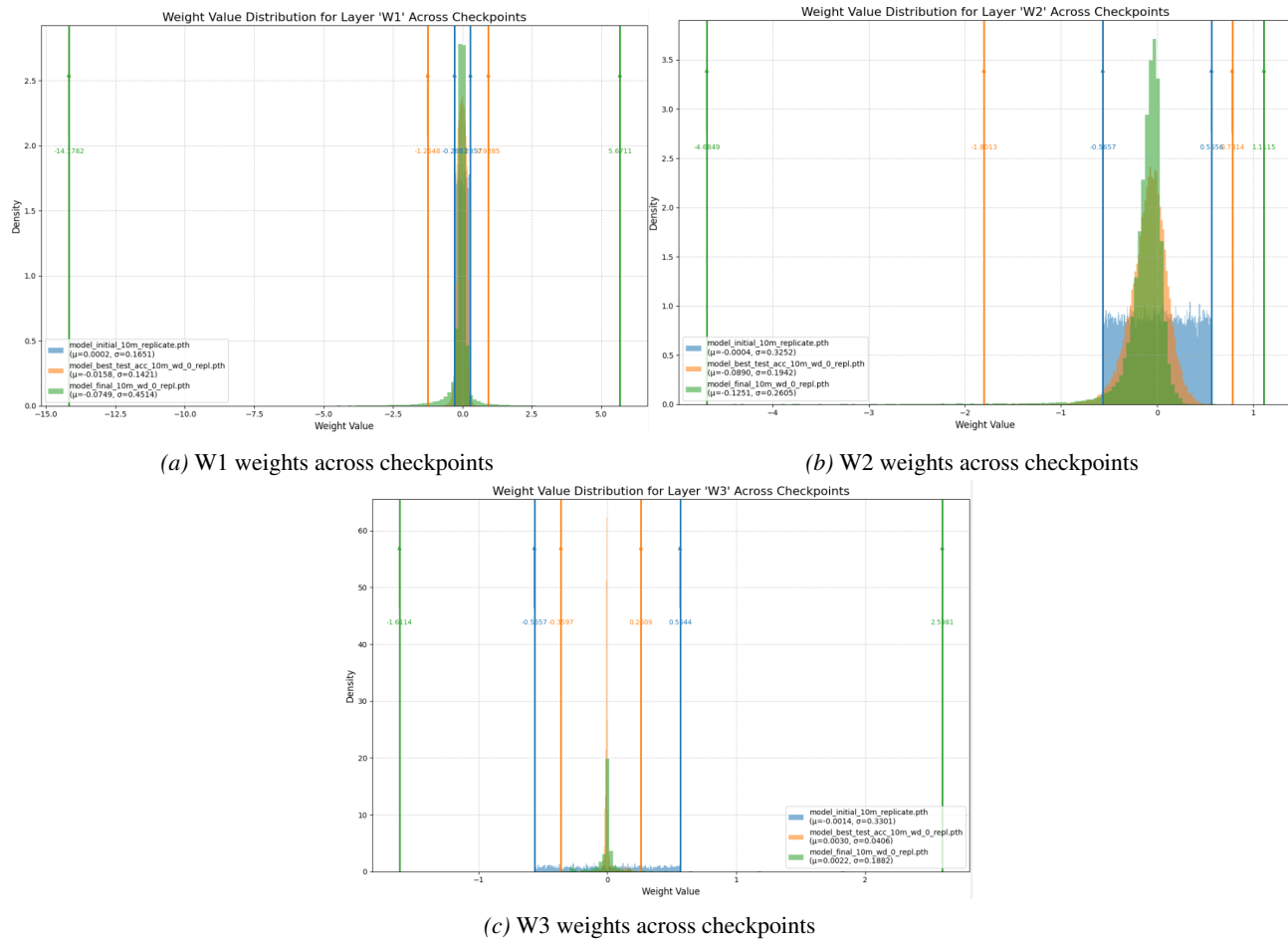


Figure 14. Weight distributions with extreme elements. Note in figures (a),(b) and (c) we see that there are structural outliers (rank-1 perturbations) causing the spikes in the randomized ESD (Correlation Traps)

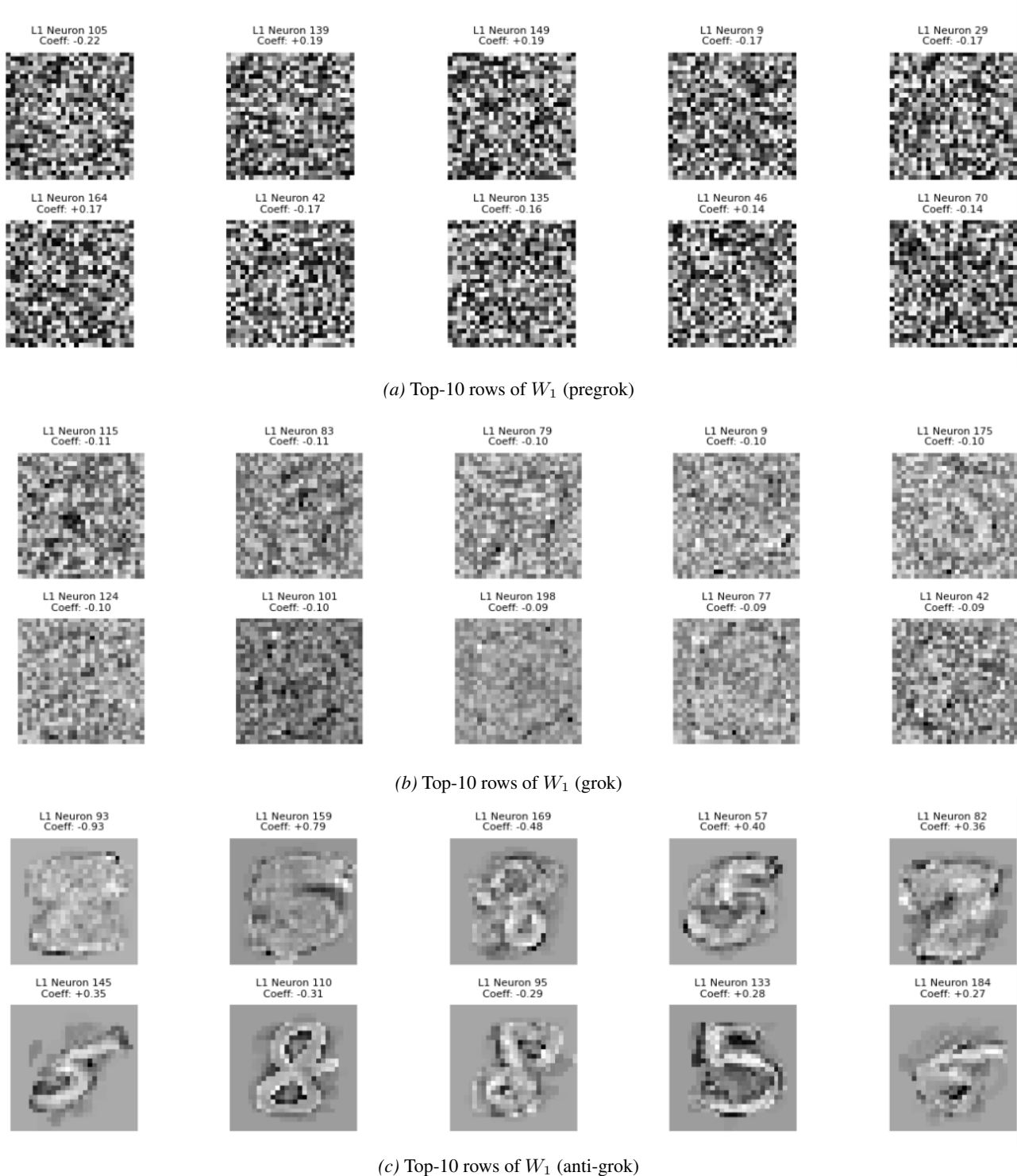


Figure 15. **Rows of W_1 (receptive fields) selected by tail vectors localization.** (a) shows noise phenotype at prerok, still diffuse at the grokking phase, but in anti-grokking the top rows look like *clear digit templates*, evidencing **digit memorization**.

H. Further Experiments: Modular Addition (predicting $x + y \bmod P$)

We additionally evaluated the HTSR diagnostics on a modular-addition task (predicting $x + y \bmod P$) with a small one-layer Transformer. The accuracy curves again exhibit the three characteristic phases (pre-grokking \rightarrow grokking \rightarrow anti-grokking), and both the HTSR exponent α and *Correlation Traps* (detected by `WeightWatcher`) flag the late-stage generalization collapse.

Hyper-parameter	Value
Layers	1
Model dimension d_{model}	128
MLP hidden size d_{mlp}	512
Heads \times head dim	4×32
Context length n_{ctx}	3
Activation	ReLU
LayerNorm	<i>disabled</i> (<code>use_ln=False</code>)
Vocabulary size	114 ($\leftarrow \text{equals_token} + 1$)

Model architecture. As predicted by HTSR, the PL-exponent α concentrates near 2 around the peak test accuracy and then deviates from 2 thereafter. Consistent with our main results, we also observe an increase in outlier eigenvalues escaping the Marchenko–Pastur bulk in multiple layers during the anti-grokking phase.

H.1. Phase and Layer-wise HTSR α for Modular Addition

Table 5. Modular addition, phase summary. Train and test accuracy (mean \pm std).

Phase	Train Acc. (mean \pm std)	Test Acc. (mean \pm std)
Pre-grok	1.0 ± 0.0	0.40 ± 0.28
Grok	1.0 ± 0.0	0.97 ± 0.02
Anti-grok	1.0 ± 0.0	0.68 ± 0.11

Table 6. Modular addition, layer-wise HTSR α across phases. Means per layer; last row reports mean \pm std across listed layers.

Layer	Pre-grok	Grok	Anti-grok
embed.embed	2.81	1.92	3.57
blocks.0.attn.W_Q	4.04	2.86	3.17
blocks.0.attn.W_K	3.99	2.00	3.20
blocks.0.attn.W_V	4.66	1.56	3.87
blocks.0.attn.out_proj	3.85	1.57	4.04
blocks.0.mlp.fc1	4.99	1.71	4.74
blocks.0.mlp.fc2	5.22	2.17	5.03
unembed.unembed	3.27	2.37	3.53
Mean\pmStd	4.10 ± 0.83	2.02 ± 0.44	3.89 ± 0.68

Interpretation. During grokking, most layers approach the *ideal* regime $\alpha \approx 2$, indicating strong, well-structured correlations and high generalization. In the anti-grokking phase, the average α drifts upward again while *selected layers* exhibit $\alpha < 2$ and clear correlation-trap outliers in their randomized spectra $X(W^{\text{rand}})$ (beyond the MP edge), as flagged automatically by `WeightWatcher`. This reproduces, on a distinct algorithmic task, the same qualitative signature reported for MNIST: α tracks all three phases, and the joint condition $\alpha \neq 2 + \text{traps}$ reliably marks late-stage generalization collapse. *Note that many of the layers in the anti-grokking phase are severely atypical, with multiple Correlation Traps, rank collapse, and even multi-model power-law signatures; for this reason, the anti-grokking α may be unreliable.*

Table 7. **Modular addition, correlation-trap counts.** Number of outlier eigenvalues (beyond the MP edge) detected by WeightWatcher in $X(W^{\text{rand}})$ for each layer and phase.

Layer	Pre-grok traps	Grok traps	Anti-grok traps
embed.embed	0.00	0.00	7
blocks.0.attn.W_Q	0.00	0.00	3
blocks.0.attn.W_K	0.00	0.00	5
blocks.0.attn.W_V	0.00	0.00	3
blocks.0.attn.out_proj	0.00	0.00	4
blocks.0.mlp.fc1	0.00	0.00	5
blocks.0.mlp.fc2	0.00	0.00	7
unembed.unembed	0.00	0.00	5
Mean±Std	0.00 ± 0.00	0.00 ± 0.00	4.88 ± 1.55

Appendix H Modular Addition: Three-phase Empirical Analysis (PRE, GROK, ANTI)

H.0 Measurement protocol and computed quantities

All computations in this appendix are performed on the above modular-addition task with modulus $p = 113$. Numeric tokens are $\{0, \dots, 112\}$ and the equals token has index 113. The model is a single-layer decoder-only transformer with $D_{\text{model}} = 128$, $D_{\text{MLP}} = 512$, $N_{\text{heads}} = 4$, $D_{\text{head}} = 32$, context length 3, ReLU activations, and no LayerNorm. For each phase label $L \in \{\text{PRE}, \text{GROK}, \text{ANTI}\}$ the following objects are computed.

(1) Keys, query, Gram spectra, and preference scores. For each head $h \in \{0, 1, 2, 3\}$:

$$\begin{aligned} K_0[x] &\in \mathbb{R}^{D_{\text{head}}} && \text{from the position-0 key on the length-3 input } [x, 0, =], \\ K_1[y] &\in \mathbb{R}^{D_{\text{head}}} && \text{from the position-1 key on } [0, y, =], \\ q_{\text{eq}} &\in \mathbb{R}^{D_{\text{head}}} && \text{from the equals-position query on } [0, 0, =]. \end{aligned}$$

Let $K^\circ[t] = K[t] - \frac{1}{p} \sum_{u=0}^{p-1} K[u]$ denote token-centering. We then define the Correlation matrices

$$G_0 = \frac{1}{D_{\text{head}}} K_0^\circ (K_0^\circ)^\top, \quad G_1 = \frac{1}{D_{\text{head}}} K_1^\circ (K_1^\circ)^\top,$$

and report the largest eigenvalues $\lambda_{\max}(G_0)$ and $\lambda_{\max}(G_1)$. Preference magnitudes use

$$s_0[x] = \frac{\langle K_0[x], q_{\text{eq}} \rangle}{\sqrt{D_{\text{head}}}}, \quad s_1[y] = \frac{\langle K_1[y], q_{\text{eq}} \rangle}{\sqrt{D_{\text{head}}}},$$

with the top-5 token indices listed by $|s_0|$ and $|s_1|$.

(2) Token-DFT energy profiles. For any token-by-feature matrix $M \in \mathbb{R}^{p \times d}$ (here $M \in \{\text{Embed, Unembed, } K_0(\text{concat}), K_1(\text{concat})\}$), let

$$W_{f,t} = \frac{1}{\sqrt{p}} e^{-2\pi i f t / p} \quad (0 \leq f, t < p), \quad F = WM, \quad \text{power}(f) = \frac{1}{d} \sum_{j=1}^d |F_{f,j}|^2.$$

The normalized energy is $E_M(f) = \text{power}(f) / \sum_g \text{power}(g)$. We report the six largest frequency indices (“top idx”), their normalized values (“vals”), and the non-DC mass $\sum_{f=1}^{p-1} E_M(f)$.

(3) Rule kernel over $\Delta = z - (x + y)$. From logits $L(x, y, z)$ (restricted to $z \in \{0, \dots, 112\}$), define

$$k(\Delta) = \frac{1}{p^2} \sum_{x,y=0}^{p-1} L(x, y, (x + y + \Delta) \bmod p) - \frac{1}{p} \sum_{\Delta'=0}^{p-1} \frac{1}{p^2} \sum_{x,y=0}^{p-1} L(x, y, (x + y + \Delta') \bmod p).$$

We list the top-6 Δ by $k(\Delta)$. We also compute $\hat{k} = Wk$ and report the top-6 frequency indices by $|\hat{k}(f)|^2$ and their powers.

H.1 Summary of accuracies and global set relations

Table 8. Accuracies and global frequency-set relations. “Kernel = Emb/Unemb freqs” indicates whether the kernel’s top-6 DFT indices match those of Emb/Unemb. “ K_0/K_1 top-6 contains DC” indicates whether index 0 appears among the top-6 for K_0/K_1 . The set $S = \{49, 64, 97, 16, 6, 107\}$ is used for intersection counts.

Phase	Train Acc.	Test Acc.	Kernel = Emb/Unemb freqs	K_0/K_1 top-6 contains DC (0)
PRE	1.0	0.13	Yes	Yes / Yes
GROK	1.0	1.0	Yes	Yes / Yes
ANTI	1.0	0.60	Yes	No / No
			$ S \cap \text{top-6}(K_0) $	$ S \cap \text{top-6}(K_1) $
			PRE	2
			GROK	5
			ANTI	6

H.2 Per-head keys, Gram largest eigenvalues, and preference indices

Table 9. Per-head $\lambda_{\max}(G_0)$, $\lambda_{\max}(G_1)$, and top-5 token indices by $|\langle q_{\text{eq}}, K \rangle|$.

Phase	Head	$\lambda_{\max}(G_0)$	$\lambda_{\max}(G_1)$	Top-5 for $ \langle q, K_0 \rangle $	Top-5 for $ \langle q, K_1 \rangle $
PRE	0	0.86	0.86	[73, 55, 38, 34, 91]	[76, 30, 9, 7, 85]
	1	1.07	1.07	[63, 79, 1, 24, 40]	[110, 32, 41, 11, 82]
	2	1.61	1.61	[76, 83, 84, 10, 73]	[83, 84, 10, 73, 51]
	3	2.09	2.09	[96, 18, 22, 110, 44]	[76, 41, 81, 40, 96]
GROK	0	1.32	1.32	[19, 40, 5, 111, 26]	[19, 40, 5, 111, 26]
	1	2.05	2.05	[78, 101, 108, 2, 85]	[78, 101, 108, 2, 85]
	2	1.56	1.56	[72, 65, 86, 79, 102]	[72, 65, 86, 79, 102]
	3	2.19	2.19	[73, 66, 50, 80, 43]	[73, 66, 50, 80, 43]
ANTI	0	123.85	123.85	[75, 98, 29, 45, 31]	[75, 98, 29, 45, 31]
	1	98.89	98.89	[71, 3, 63, 70, 94]	[71, 3, 63, 70, 94]
	2	123.01	123.01	[72, 5, 56, 93, 6]	[72, 5, 56, 93, 6]
	3	94.14	94.14	[4, 80, 58, 11, 103]	[4, 80, 11, 58, 103]

H.3 Token–DFT energy (dominant indices and non-DC mass)

H.4 Rule kernel $k(\Delta)$ and its discrete Fourier spectrum

Cross-phase observations (data-derived). Across all phases, the dominant frequency indices for Emb/Unemb and the kernel coincide with $S = \{49, 64, 97, 16, 6, 107\}$. For K_0 and K_1 , the top-6 intersections with S are (2, 2) in PRE, (5, 5) in GROK, and (6, 6) in ANTI. The top-5 preference token lists for $|\langle q_{\text{eq}}, K_0 \rangle|$ and $|\langle q_{\text{eq}}, K_1 \rangle|$ are identical for every head in GROK; they differ on all heads in PRE; in ANTI they are identical on heads 0–2 and contain the same five tokens in a different order on head 3.

H.6 Embedding/Unembedding Fourier profiles (overlay) and comparison across phases

Figures 16–17 plot the normalized token–DFT energy $E_M(f)$ for the Emb/Unemb matrices for the three phases. The horizontal axis is the frequency index $k \in \{0, \dots, 112\}$; the vertical axis is the normalized power $E_M(k)$ as defined in Section H.0(2).

Quantitative check (from Tables 10 and 11). All three phases share the same six non-DC indices for Emb/Unemb

Late-Stage Generalization Collapse in Grokking

Table 10. Top-6 DFT and normalized energies for the token-indexed matrices, with non-DC mass. Indices are in $\{0, \dots, 112\}$.

Phase	Module	Top idx (in reported order)	Values for top idx (same order)	non-DC mass
PRE	Embed	[49, 64, 97, 16, 6, 107]	[0.0667, 0.0667, 0.0509, 0.0509, 0.0200, 0.0200]	1.000
	Unembed	[49, 64, 97, 16, 6, 107]	[0.0714, 0.0714, 0.0484, 0.0484, 0.0222, 0.0222]	1.000
	K_0	[0, 104, 9, 64, 49, 20]	[0.6845, 0.0180, 0.0180, 0.0130, 0.0130, 0.0080]	0.315
	K_1	[0, 104, 9, 64, 49, 20]	[0.7011, 0.0170, 0.0170, 0.0123, 0.0123, 0.0076]	0.299
GROK	Embed	[49, 64, 97, 16, 6, 107]	[0.2181, 0.2181, 0.1270, 0.1270, 0.1015, 0.1015]	1.000
	Unembed	[49, 64, 97, 16, 6, 107]	[0.2144, 0.2144, 0.1438, 0.1438, 0.1405, 0.1405]	1.000
	K_0	[49, 64, 0, 97, 16, 6]	[0.3660, 0.3660, 0.1076, 0.0757, 0.0757, 0.0039]	0.892
	K_1	[49, 64, 0, 97, 16, 6]	[0.3658, 0.3658, 0.1081, 0.0757, 0.0757, 0.0039]	0.892
ANTI	Embed	[49, 64, 97, 16, 6, 107]	[0.0210, 0.0210, 0.0206, 0.0206, 0.0199, 0.0199]	0.992
	Unembed	[49, 64, 97, 16, 6, 107]	[0.0264, 0.0264, 0.0218, 0.0218, 0.0201, 0.0201]	0.992
	K_0	[16, 97, 107, 6, 49, 64]	[0.0260, 0.0260, 0.0230, 0.0230, 0.0224, 0.0224]	0.985
	K_1	[16, 97, 107, 6, 49, 64]	[0.0260, 0.0260, 0.0230, 0.0230, 0.0224, 0.0224]	0.985

Table 11. Top-6 Δ for $k(\Delta)$ and the top-6 DFT frequencies of k with powers $|\hat{k}(f)|^2$.

Phase	Top-6 Δ (in reported order)	Top-6 DFT freqs (idx) with powers (same order)
PRE	[0, 7, 106, 14, 99, 21]	idx [49, 64, 97, 16, 6, 107]; pow [88, 713.516, 88, 713.516, 8, 677.078, 8, 677.078, 61.569, 61.569]
GROK	[0, 37, 76, 92, 21, 99]	idx [49, 64, 97, 16, 6, 107]; pow [208, 933.61, 208, 933.61, 10, 937.356, 10, 937.356, 4, 895.602, 4, 895.602]
ANTI	[0, 21, 92, 76, 37, 99]	idx [49, 64, 97, 16, 6, 107]; pow [9, 955.823.0, 9, 955.823.0, 1, 597, 666.1, 1, 597, 666.1, 1, 207, 065.4, 1, 207, 065.4]

Note on index pairs. With $p = 113$, the frequency indices occur in complementary pairs $(f, 113 - f)$; the sets $\{49, 64\}$, $\{97, 16\}$, $\{6, 107\}$ satisfy $64 = 113 - 49$, $97 = 113 - 16$, and $107 = 113 - 6$.

Unembed: [49, 64, 97, 16, 6, 107]. Peak magnitudes at these indices differ: *Embed* peaks are ≈ 0.218 (GROK), ≈ 0.067 (PRE), ≈ 0.021 (ANTI); *Unembed* peaks are ≈ 0.214 (GROK), ≈ 0.071 (PRE), ≈ 0.026 (ANTI). Hence GROK is highly concentrated on the six-rule frequency set, PRE shows the same set with smaller peaks, and ANTI exhibits a broadband profile (same indices but low peak-to-background ratios).

Relation to key banks. For ANTI, K_0 and K_1 are not broadband: their top-6 frequency indices are exactly the six non-DC rule indices with non-DC mass 0.985 (Table 10). Thus ANTI combines keys tightly supported on the rule frequencies with embeddings/unembedding that are comparatively broadband. This mismatch is visible in Figures 16–17.

Interpretation

- From the per-head preference lists and Gram spectra (Table 9), **PRE** lacks the position-symmetry expected of modular addition; **GROK** exhibits exact symmetry; **ANTI** exhibits the same symmetry with much larger key-bank variance.

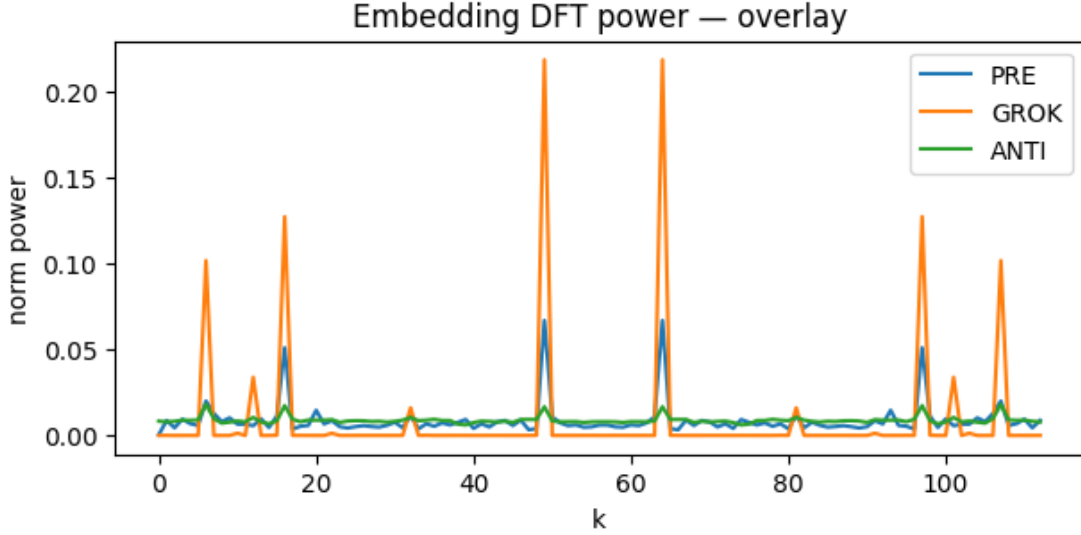


Figure 16. **Embedding DFT power (overlay).** Dominant nonzero frequencies are the complementary pairs $\{49, 64\}$, $\{97, 16\}$, $\{6, 107\}$. The GROK trace shows sharp peaks; PRE shows smaller peaks; ANTI appears comparatively broadband with shallow peaks at the same indices.

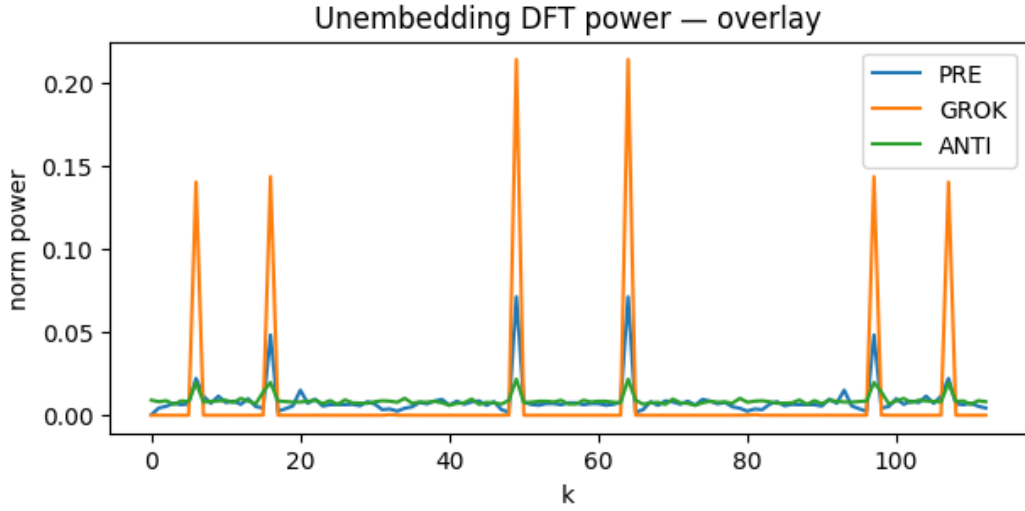


Figure 17. **Unembedding DFT power (overlay).** Same six nonzero frequencies as in the embedding. GROK is sharply peaked, PRE is weaker, and ANTI is comparatively broadband.

- Therefore, **ANTI**'s failure cannot be attributed to attention key–query architecture; it must arise elsewhere as we show below.
- **Embedding/Unembedding Fourier profiles (Tables 10 and 11, Figs. 16–17).** All phases share the same six non-DC indices $\{49, 64, 97, 16, 6, 107\}$ for Embed and Unembed, but the peak magnitudes differ sharply: *Embed* peaks are approximately:

GROK: [0.2181, 0.2181, 0.1270, 0.1270, 0.1015, 0.1015]

PRE: [0.0667, 0.0667, 0.0509, 0.0509, 0.0200, 0.0200]

ANTI: [0.0210, 0.0210, 0.0206, 0.0206, 0.0199, 0.0199]

Unembed peaks show the same ordering:

GROK: [0.2144, 0.2144, 0.1438, 0.1438, 0.1405, 0.1405]

PRE: [0.0714, 0.0714, 0.0484, 0.0484, 0.0222, 0.0222]

ANTI: [0.0264, 0.0264, 0.0218, 0.0218, 0.0201, 0.0201].

Thus, while the six frequencies are present in all phases, **ANTI** exhibits a comparatively *broadband* Embed/Unembed profile (low peak-to-background), in contrast to the sharp, high-amplitude lines in **GROK**.

- **Kernel vs. embedding contrast.** The rule kernel $k(\Delta)$ has the same six-frequency support in all phases, and its top-line powers are largest in **ANTI**:

ANTI: [9955823.0, 9955823.0, 1597666.1, 1597666.1, 1207065.4, 1207065.4]

GROK: [208933.61, 208933.61, 10937.356, 10937.356, 4895.602, 4895.602]

PRE: [88713.516, 88713.516, 8677.078, 8677.078, 61.569, 61.569]

Hence, even though the rule kernel (and the keys) are strongly aligned to the six-rule frequencies in **ANTI**, the Embed/Unembed spectra *lose the sharp Fourier spikes* and appear broadband.

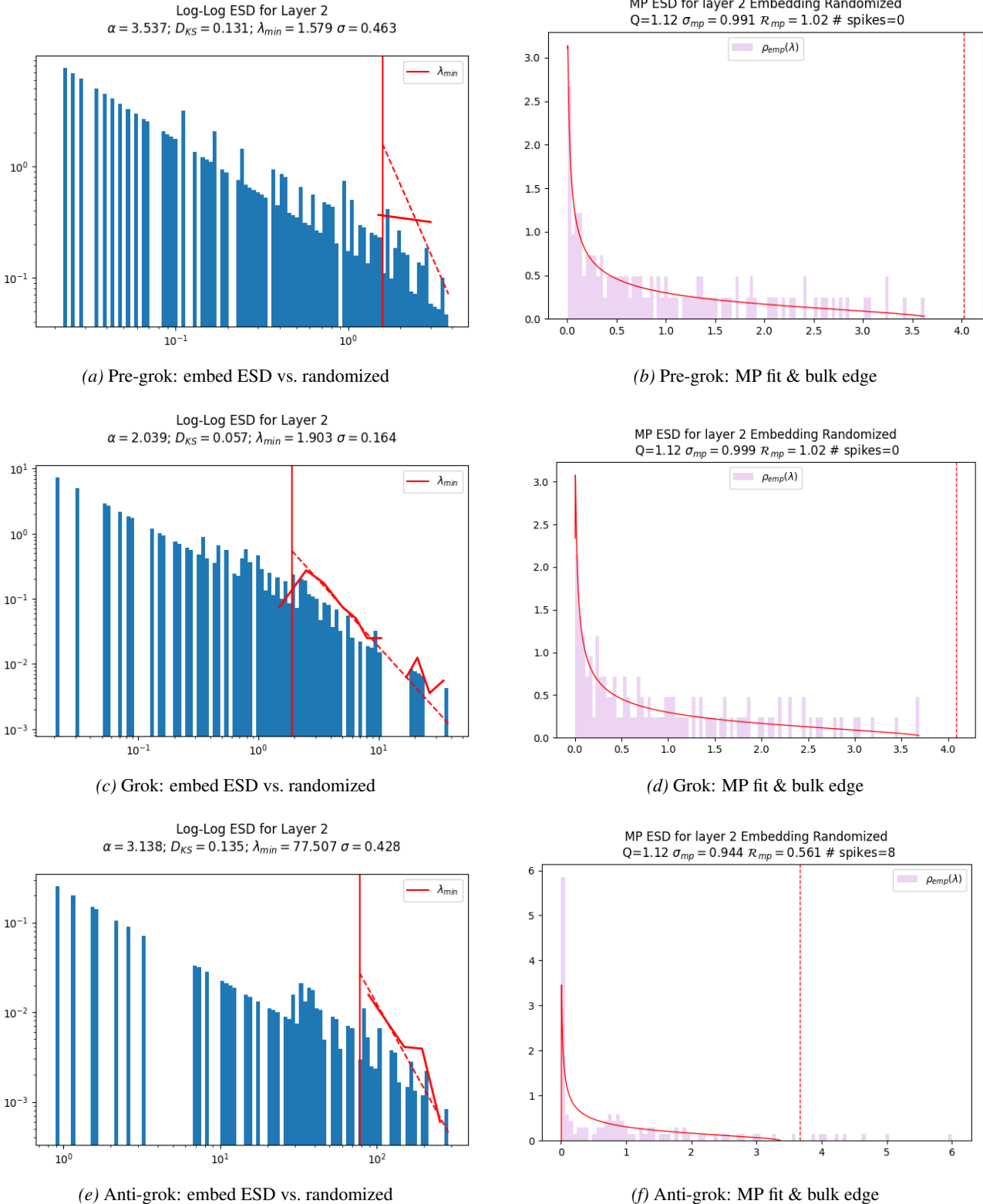


Figure 18. Embedding-layer ESD across phases (3×2 grid). For each phase (rows), the left panel shows the empirical spectral density (ESD) for $\mathbf{W}_{\text{embed}}$ (blue) on a log-log scale, along with the best PL fit of the tail (red), and the associated α and other metrics for the fit. The right panel shows the Marchenko–Pastur (MP) fit of the ESD of the randomized matrix $\mathbf{W}_{\text{embed}}^{\text{rand}}$ and the far edge of the Tracy–Widom (TW) fluctuations (dotted vertical line). For all the Figures on the left, (a), (c), and (e), show distinct power law (PL) behavior across the entire ESD, not just the tail, which has its own, separate PL fit. This is highly unusual, and indicates strong overfitting even in the presence of correlated learning. In the grokking phase, Figure (c) shows a very good PL fit of the tail, with $\alpha \approx 2$, and a much smaller D_{KS} value than in the other 2 phases. Coming to the right panel, for both the pre-grokking and grokking phases, in Figures (b) and (d), the MP theory (red line) is a very good fit to the randomized ESDs (pink). In contrast, in Figure (f), in the anti-grokking phase, the randomized ESD (pink) is extremely atypical. The MP fit of the bulk region is not very good, there are several Correlation Traps (are eigenvalues extending far beyond the randomized MP bulk edge ($\lambda_{trap} \gg \lambda_{rand}^+$)), and there is also significant rank collapse (larger density at zero than the MP theory predicts). Here, anti-grokking appears to correspond to catastrophic forgetting.

I. Perturbation studies and our metrics

We try modulating the rescaling alpha to 4 we find in particular, even when the parameters are globally rescaled (a simple perturbation inspired by Omnigrok-style analyses), the Weightwatcher layer quality metrics track the grokking phases.

Protocol and phase definitions. The phase boundaries change as follows : *pre-grok* (10^2 – 5×10^4 steps), *grok* (5×10^4 – 5×10^5 steps), and *anti-grok* ($> 5 \times 10^5$ steps). For each phase, we evaluate training/test accuracy and the global parameter ℓ_2 norm. We additionally report layer-wise heavy-tail exponents (WeightWatcher α) and a layer-wise correlation-trap statistic. All values are reported as mean \pm standard deviation over the samples used within each phase.

Table 12. Accuracy by phase. Mean \pm std training and test accuracy within each phase.

Phase	Train Accuracy (mean \pm std)	Test Accuracy (mean \pm std)
Pre-grok	0.7298 ± 0.0408	0.4926 ± 0.0187
Grok	1.0000 ± 0.0000	0.8879 ± 0.0051
Anti-grok	1.0000 ± 0.0000	0.6184 ± 0.1086

Table 13. Global ℓ_2 norm by phase. Mean \pm std of the parameter ℓ_2 norm within each phase.

Phase	WeightNorm (mean \pm std)
Pre-grok	17.52 ± 0.00
Grok	16.80 ± 0.22
Anti-grok	27.64 ± 8.39

Table 14. Layer-wise α across phases. WeightWatcher heavy-tail exponent estimates (α) summarized within each phase. Phase windows are: pre-grok (10^2 – 5×10^4), grok (5×10^4 – 5×10^5), anti-grok ($> 5 \times 10^5$).

Layer	Pre-grok mean	Grok mean	Anti-grok mean
Layer 1	8.88	2.59	1.23
Layer 2	3.84	2.77	1.49
Mean \pm Std	6.36 ± 2.52	2.68 ± 0.09	1.36 ± 0.13

Table 15. Correlation-trap analysis (layer-wise). A layer-wise correlation-trap statistic summarized by phase (mean \pm std over samples in each phase).

Layer	Pre-grok	Grok	Anti-grok
1	0.00	0.00	7.00
3	0.00	0.00	1.17
5	0.00	0.00	5.50
Mean \pm Std	0.00 ± 0.00	0.00 ± 0.00	4.56 ± 3.03